CANADIAN THESES

THÈSES CANADIENNES

NOTICE

The quality of this microfiche is heavily dependent upon the quality of the original thesis submitted for microfilming. Every effort has been made to ensure the highest quality of reproduction possible.

If pages are missing, contact the university which granted the degree.

Some pages may have indistinct print especially if the original pages were typed with a poor typewriter ribbon or if the university sent us an inferior photocopy.

Previously copyrighted materials (journal articles, published tests, etc.) are not filmed.

Reproduction in full or in part of this film is governed by the Canadian Copyright Act, R.S.C. 1970, c. C-30.

AVIS

La qualité de cette microfiche dépend grandement de la qualité de la thèse soumise au microfilmage. Nous avons tout fait pour assurer une qualité supérieure de reproduction.

S'il manque des pages, veuillez communiquer avec l'université qui a conféré le grade.

La qualité d'impression de certaines pages peut laisser à désirer, surtout si les pages originales ont été dactylographiées à l'aide d'un ruban usé ou si l'université nous a fait parvenir une photocopie de qualité inférieure.

Les documents qui font déjà l'objet d'un droit d'auteur (articles de revue, examens publiés, etc.) ne sont pas microfilmés.

La reproduction, même partielle, de ce microfilm est soumise à la Loi canadienne sur le droit d'auteur, SRC 1970, c. C-30.

THIS DISSERTATION
HAS BEEN MICROFILMED
EXACTLY AS RECEIVED

LA THÈSE A ÉTÉ
MICROFILMÉE TELLE QUE
NOUS L'AVONS REÇUE

TWO-PHOTON PHOTOVOLTAIC EFFECT IN Cu_2O

by
Daniel R. Venasse

Thesis submitted to
the School of Graduate Studies
in partial fulfillment of the requirements
for the degree of
Master of Science in Physics

Department of Physics
Faculty of Science
University of Ottawa
Ottawa, Canada
1986

ISBN 0-315-36555-2

UNIVERSITÉ D'OTTAWA
UNIVERSITY OF OTTAWA

ABSTRACT

The study of excitons and two-photon absorption was performed in cuprous oxide. A technique was developed to produce single crystals of Cu_2O. These crystals were then analyzed at low intensity to determine, by transmission, the energies of the exciton transitions as a function of temperature. Furthermore, Schottky barrier Cu_2O/Cu photovoltaic effect samples were produced by thermal oxidation of copper. One-photon measurements were performed with these samples to study the behaviour of the exciton lines as the temperature was varied. Two-photon absorption experiments were then performed using an optical parametric oscillator pumped by a dye laser in an attempt to observe the one-photon parity forbidden transitions in the exciton region. Modelling of the two-photon photovoltaic effect reproduces the observed results and reinforces their interpretation.

ACKNOWLEDGMENTS

I would like to thank my supervisor, Dr. Bernard. The considerable assistance provided to me by Dr. Fortin during this project is greatly appreciated. I also appreciate the kindness and patience shown to me by all the other professors over the years. I would also like to thank Mike Jackson and the secretaries as well as the store and workshop employees who did their best to keep things running smoothly. Special thanks to Bob Hart for his help and advice. As well, the help and friendship provided by the other students will not be forgotten.

I am very grateful for the financial assistance provided by the Natural Sciences and Engineering Research Council of Canada.

Most important of all, I would like to thank my parents for all that they have done for me.

TABLE OF CONTENTS

LIST OF FIGURES

CHAPTER I INTRODUCTION

Cuprous oxide (Cu_2O) has been studied for many years because of the structure it displays at its fundamental absorption edge. To excite an electron from the valence band to the conduction band requires a photon of energy equal to or greater than the energy gap of the semiconductor. In Cu_2O, a photon of energy less than the bandgap energy can also be absorbed, creating a bound electron-hole pair referred to as an exciton. The energy of this bound system is less than that of a system with an electron in the conduction band and a hole in the valence band in the same way that a hydrogen atom is in a lower energy state than a free electron and proton.

The binding energy of the exciton is quantized and it depends on the exciton's n value as well as its angular momentum l. Transitions to some of these levels are allowed by the selection rules, while others are forbidden.

The study of two-photon absorption spectra is a very useful tool for the investigation of the excitons in Cu_2O. It is an elementary excitation process in which two photons are simultaneously absorbed. It provides a wealth of new information about the exciton series because of its different selection rules. One-photon forbidden transitions become allowed with two photons and one-photon allowed transitions become forbidden. Therefore, any particular transition should be visible using one technique or the other.

In order to detect the two-photon absorption taking place in the sample, it is important that the one-photon absorption at the exciting energy be as small as possible. This is especially important since two-photon absorption is a second order effect. Lasers are used to observe two-photon absorption because of the high intensities that they provide. Usually

two sources are used, one a fixed wavelength laser, the other a variable wavelength low intensity source. Instead of two separate sources, an optical parametric oscillator pumped by a dye laser was used as a tunable source for the two-photon absorption experiments done for this thesis.

Of course, the visibility of the exciton lines in the spectra depends greatly on the quality and characteristics of the samples. Low quality samples display poor exciton structure in their spectra. Furthermore, the samples must be thin for transmission measurements because of the relatively high absorption coefficient in this spectral region. This requires that the samples be carefully polished to grind away material until they are thin enough or (as everyone who has polished samples before knows) until they get broken. The samples used for the transmission measurements were grown by thermal oxidation of copper. Exciton lines up to n=3P were visible in the transmission spectra.

The photovoltaic effect in Cu_2O/Cu Schottky barrier cells was another technique used to observe the excitons. Extensive interest in the photovoltaic properties of these devices existed in the 1930's. They were in fact the first in which the photovoltaic effect was explained[1].

For this type of device it is much simpler to produce a layer of cuprous oxide that is a few ten's of microns thick. Furthermore, the oxidation period consists of a few seconds instead of a few days and no polishing of the oxide is required. Also, the oxide layer is supported by the copper substrate on which it is grown, making it much less fragile. Exciton lines up to n=4P could easily be seen in this type of sample.

This project started off as an attempt to observe two-photon absorption in Cu_2O/Cu

photovoltaic effect samples. This approach was initially dropped because a one-photon signal produced by the photoexcitation of carriers from the copper substrate was being detected. Suggestions that another metal be substituted for the copper to form the Schottky barrier produced some hope for the use of this technique. Unfortunately, previous research[2] showed that most metals reduce Cu_2O to form essentially a Cu_2O/Cu contact. At this point, it was decided to abandon this technique in favor of transmission measurements.

Several techniques were attempted to produce single crystals of Cu_2O. After much development, a technique consisting of the slow oxidation of single crystals of copper proved capable of consistently producing single crystals of cuprous oxide. Several one-photon experiments were performed to measure the position of the excitons and their shift with temperature.

At this point, the possibility of applying a bias voltage to the photovoltaic effect samples in order to reduce the one-photon signal resulted in a return to this technique. The high intensity measurements were all performed on samples of this type

This thesis will be divided into four major chapters. The first of these, Chapter II, will introduce some exciton theory and the rules governing the transitions that can take place to the various energy levels. This will be followed by an introduction to the photovoltaic effect in Schottky barrier devices and the effect of an electric field. Chapter III will deal with the oxidation apparatus and the techniques used to produce the samples used for transmission and photovoltaic effect experiments. In Chapter IV, the equipment required to perform the various experiments will be described, with emphasis placed on the cryostats and the optical parametric oscillator. The results obtained from the various

experiments will be presented and discussed in Chapter V. The thesis will conclude with a brief summary and conclusion.

CHAPTER II THEORY

II.1 INTRODUCTION

What is an exciton? In a semiconductor with a bandgap energy E_G, a photon of sufficient energy can excite an electron from the valence band to the conduction band. This band-to-band transition has a lowest energy limit $h\nu_\infty = E_G$. The electron in the conduction band and the hole in the valence band are "free". Frenkel[3] and later Peierls[4] suggested that photons of energy $< E_G$ could create electrons and holes in a bound state in which a small coulomb interaction exists between them. This bound state corresponds to an excited state of the crystal and is called an EXCITON. This chapter deals with the basic theory underlying one and two-photon transitions to exciton levels. The specific case of Cu_2O will be discussed. Also in this chapter is an introduction to Schottky barrier devices and Cu_2O/Cu photovoltaic cells. As well, the effect of an electric field on excitons in such a device will be discussed. These concepts are introduced here so that the experimental results presented in later chapters may be better understood.

II.2 ELEMENTARY THEORY

The first thing to discuss is the exciton energy levels. The binding energy of an exciton is quantized as for the hydrogen atom, so that it has a well defined set of energy states. The mechanism for creation of bound pairs corresponds to a series of sharp absorption lines converging to the band-to-band absorption energy limit $h\nu_\infty = E_G$ (Figure II.1).

The Bohr theory of the hydrogen atom may be readily modified to take into account both the dielectric constant of the medium and the effective masses of the electron and

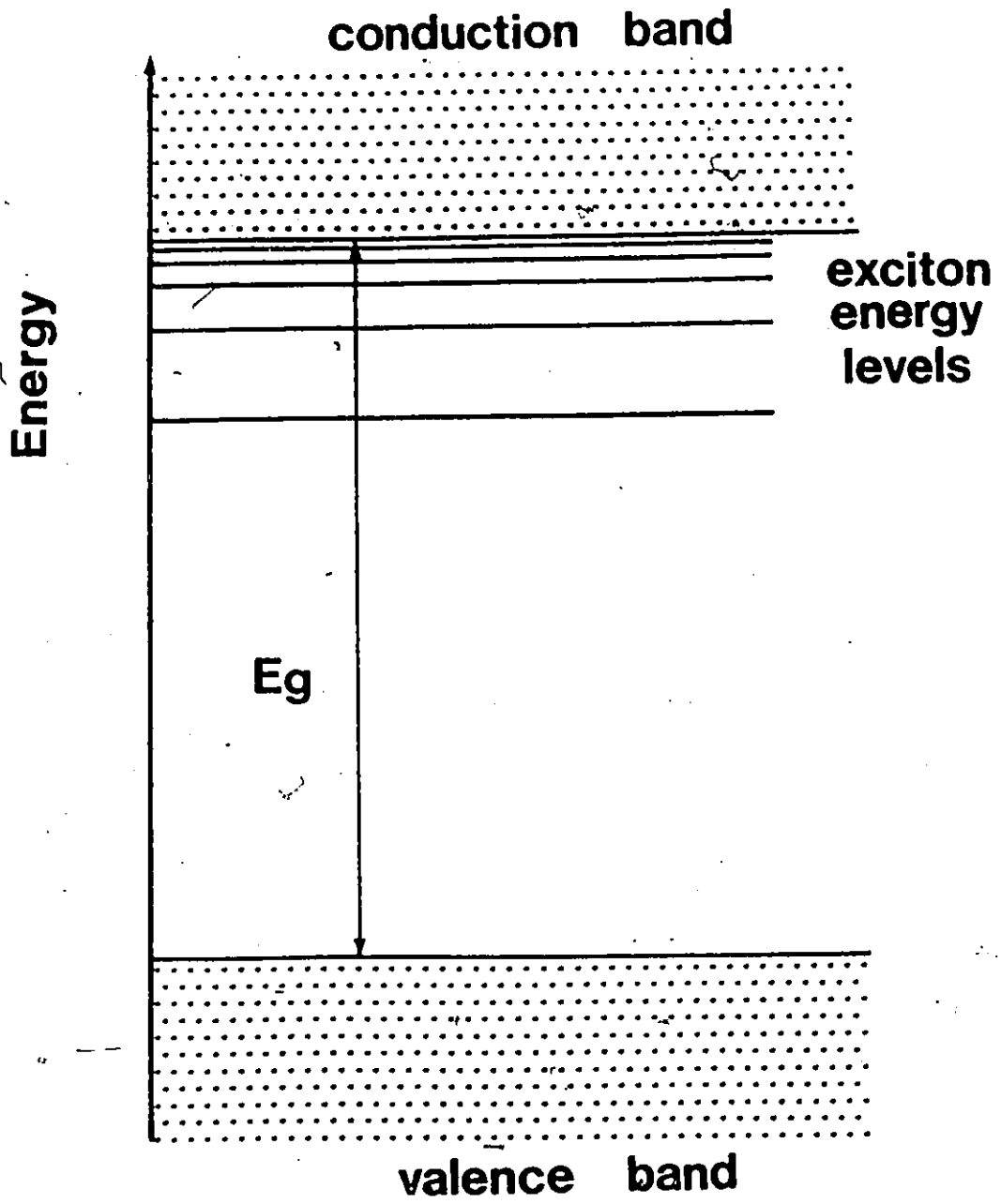

FIGURE II.1 Diagram of exciton energy levels

hole for an exciton. The binding energy of the exciton is typically 100 to 1000 times lower than the binding energy of the hydrogen atom. Because the bond is weak, the mean distance between the electron and the hole will be 1 or 2 orders of magnitude larger than the diameter of the hydrogen atom; it can range over many spacings of the crystal lattice. The binding energy of the Cu_2O $n = 1S$ yellow series exciton is 0.14 eV and its radius is 10 Å. (For comparison, the binding energy of the hydrogen atom is 13.6 eV and its radius is 0.5 Å). Because the exciton radius is larger than the typical atomic spacing of 3 to 5 Å, the dielectric constant of the semiconductor, ϵ, must be introduced. The value of e^2/r is replaced by $e^2/(\epsilon r)$. Also, the mass of the electron, m_e must be replaced by μ, the effective mass of the exciton, where $1/\mu = 1/m_e^* + 1/m_h^*$, m_e^* being the effective mass of the electron and m_h^* the effective mass of the hole. This is because the hole mass is much closer to the electron mass than the proton mass is in the hydrogen case.

Now

$$R = \frac{1}{(4\pi\epsilon_0)^2}\frac{e^4 m_e}{4\pi\hbar^3 c} \tag{1}$$

where R is the Rydberg constant and ϵ_0 is the permittivity of free space.

$$R' = \frac{1}{(4\pi\epsilon_0)^2}\frac{(e^4/\epsilon^2)m_e(\mu/m_e)}{4\pi\hbar^3 c} \tag{2}$$

$$R' = \frac{1}{(4\pi\epsilon_0)^2}\frac{e^4 m_e}{4\pi\hbar^3 c}\frac{\mu}{\epsilon^2 m_e} \tag{3}$$

$$R' = R \times \frac{\mu}{\epsilon^2 m_e} \tag{4}$$

where R' is the Rydberg exciton constant.

If E_c is the lowest energy level of the conduction band, and the zero point energy is

set at the top of the valence band, the energies of the exciton levels are given by

$$E_n = E_c - \frac{R'ch}{n^2} \tag{5}$$

This equation has the same form as Bohr's expression for the allowed bound energy states of the hydrogen atom:

$$E_n = \frac{Rch}{n^2} \tag{6}$$

As n gets larger, $R'ch/n^2$ becomes quite small. The exciton's energy levels converge toward a high energy limit, which is equal to the energy gap of the semiconductor. For $h\nu > h\nu_\infty$, the absorption spectra is a continuum and corresponds to band-to-band transitions.

It is possible for several exciton series to occur in the same semiconductor. They are the result of excitonic transitions between different sets of bands, so that they occur at different energies and are observed in different regions of the spectrum.

II.3 MORE EXCITON THEORY

The non-degeneracy of exciton energy levels and the transitions to these various levels must now be considered. The degeneracy of exciton levels of different l symmetry with the same n value which exists in the spherical symmetry approximation is removed by the internal crystal field as well as by exciton-phonon interaction[5]. For a semiconductor with forbidden direct one-photon transitions at the Γ-point of the Brillouin zone, dipole absorption to the corresponding exciton levels is forbidden by symmetry. Transition to S and D-type exciton levels are strongly forbidden and their oscillator strength can only be due to electrical quadrupolar transitions[6,7,8]. However, transitions leading to P-type excitons (referred to as second-class transitions) are only weakly forbidden, and still correspond

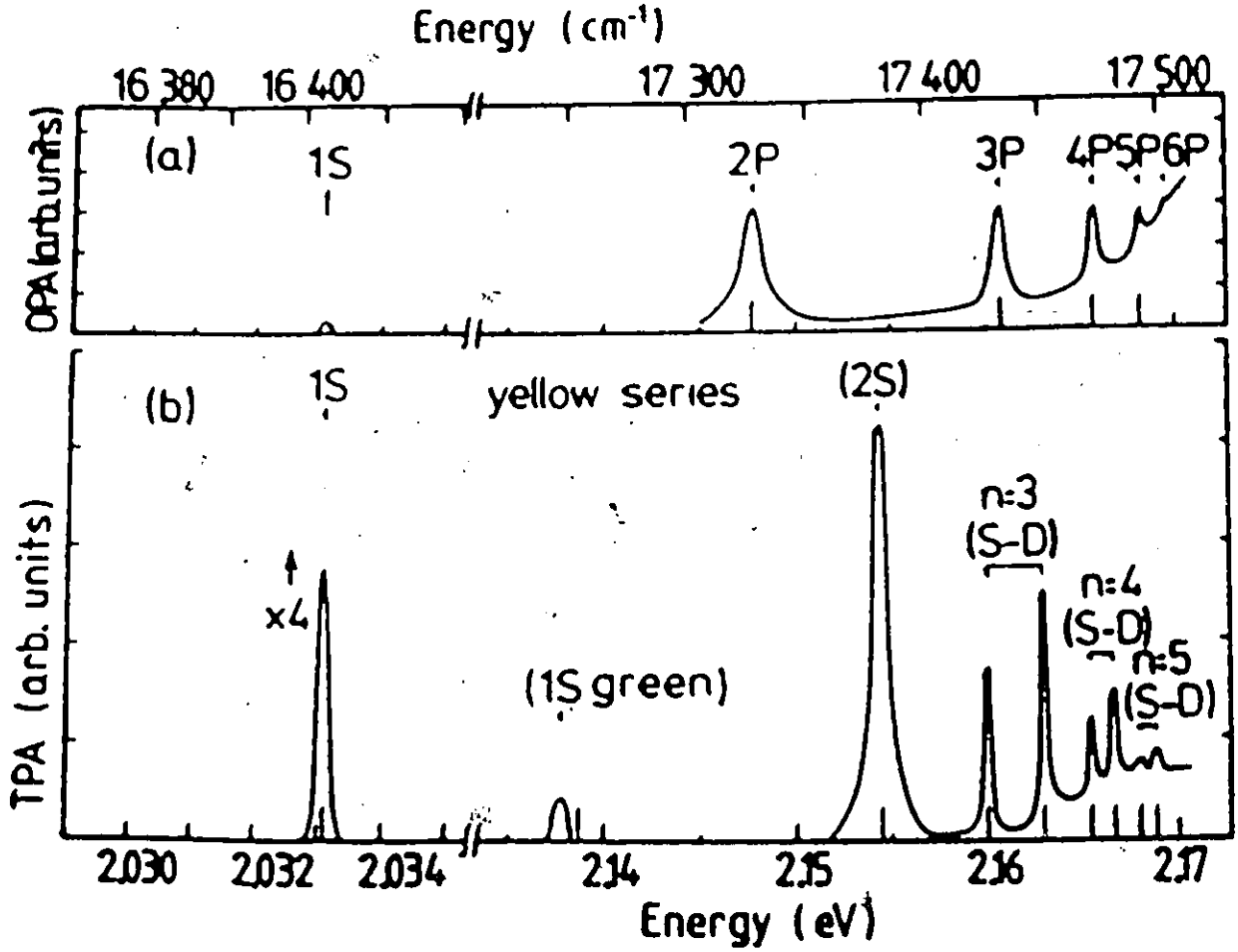

FIGURE II.2 One and two-photon absorption spectra of Cu_2O at 4.2 K[8]

to the dipole approximation[9]. They are the ones that will be observed in the absorption spectra of a semiconductor with forbidden direct one-photon transitions (Figure II.2*a*).

At this point, the concept of two-photon absorption is introduced. The process is one in which two quanta are simultaneously absorbed in an electronic transition. The energy sum of the two quanta must be equal to the energy of the electronic transition. In the case of simultaneous absorption of two photons, the two photons can be of equal or different energies, but each is less than the band-gap energy. In this case the intermediate state is a virtual state and does not require the presence of impurities[10]. Of great importance is that the selection rules are different than for one-photon absorption. Transitions between states of the same parity that were symmetry forbidden with one photon become allowed with two photons and vice-versa[11]. Therefore, the S and D lines of the exciton series will become the ones that can be seen in the spectra of the samples[12] (Figure II.2*b*).

Now, multiphoton absorption can be described in a phenomenological manner by the generalized Beer-Lambert law[13]:

$$\frac{dI}{dx} = -\sum_m \alpha_m I^m \tag{7}$$

where α_m is the m-photon absorption coefficient expressed in units of $(\text{length})^{2m-3}/(\text{power})^{m-1}$, I is the light intensity in watts per square meter, and x is the propagation direction. One and two-photon transitions are the ones of interest here so that

$$\frac{dI}{dx} = -\alpha_1 I - \alpha_2 I^2 \tag{8}$$

In order to observe the effects of two-photon absorption, the one-photon contribution should obviously be as small as possible. This is even more important when the second

term is relatively small. To help matters, lasers are used because of the high light intensities they can provide.

Since the two-photon absorption is directly proportional to the intensity of the laser beam, its magnitude can be controlled by adjusting the laser intensity. This permits one to measure a large variation of two-photon transition rates using the largest available single crystals. In contrast, the only way of measuring one-photon absorption spectra in regions of strong absorption lies in using very thin samples, which are usually difficult to obtain. Further, unlike the experiments measuring reflectivity or those measuring absorption in thin samples, two-photon absorption experiments are affected much less by surface properties of the sample[14]. The properties revealed are those of the volume of the crystal rather than just the skin depth.

How does the absorption coefficient for a two-photon band-to-band transition vary as a function of the wavelength of the incident light? It is expected to vary rapidly when the energy of the two photons approaches the energy of band-to-band transitions. The form of the variation depends on many factors. Theoretically, this highly non-linear process has been studied within the framework of perturbation theory, or by the 'non-perturbative' approach suggested by Keldysh in 1964[15]. A 'non-perturbative' scheme similar to Keldysh's has since been applied to calculate multi-photon transition rates in direct gap crystals for arbitrarily large intensities[16]. For linearly polarized light, the expression for the two-photon absorption coefficient is

$$\alpha_2 = \frac{2^{7/2}\pi e^4}{c^2}\frac{(\mu)^{3/2}}{m_e^2 n^2}\frac{1}{E_G^{5/2}(T)}\left(\frac{2x-1}{x^5}\right)^{3/2} \qquad (9)$$

where $x = \hbar\omega/E_G(T)$, m_e is the electron effective mass of the conduction band, μ is the

reduced effective mass, defined by $(\mu)^{-1} = (m_e)^{-1} + (|m_h|)^{-1}$, m_h is the effective mass of the valence band, and n is the refractive index of the crystal.

Now, for two-photon absorption near the band edge, $\hbar\omega \simeq E_G/2$. For $\hbar\omega > E_G/2$, the value of $\left(2(\hbar\omega/E_G) - 1\right)^{3/2}$ can be calculated. For $\hbar\omega < E_G/2$, a problem occurs since the value inside the parentheses becomes negative. A *width* δ, of Lorentzian type, can be introduced by adding a term $i\delta$ to E_G[17]; α_2 is obtained from the real part of the expression, giving

$$\alpha_2 = C\frac{E_G^{7/2}}{(h\nu)^{15/2}}\left\{(2h\nu - E_G)\left[\left[(2h\nu - E_G)^2 + \delta^2\right]^{1/2} + (2h\nu - E_G)\right]^{1/2} + \delta\left[\left[(2h\nu - E_G)^2 + \delta^2\right]^{1/2} - (2h\nu - E_G)\right]^{1/2}\right\} \tag{10}$$

where C is a constant depending on the electron charge e, the speed of light, the effective masses and the index of refraction of the crystal.

II.4 CUPROUS OXIDE

In this section, it is time to discuss the more specific case of Cu_2O. Cuprous oxide is a p-type semiconductor. No technique has yet been devised to produce n-type Cu_2O[2]. Its crystal structure is simple cubic[18], with a center of symmetry. Its band structure permits the creation by light of four different exciton series: yellow, green, indigo, and blue[19]. In the yellow part of the spectrum at 4.2 K, the direct band-to-band one-photon transitions at the Γ point ($k = 0$) are weakly forbidden and are accompanied by P-state excitons of the yellow exciton series. When studied by the two-photon technique, the S and D exciton lines become visible in the spectra. The yellow series is the one that will be studied using both one and two-photon techniques.

As the temperature of the sample is varied, the position and shape of the exciton lines change. At room temperature the thermal phonon energy ($\simeq$ 0.025 eV) is enough to overwhelm the weak excitonic bond[20]. The n=2P exciton has a binding energy of about 0.024 eV, and all the excitons of higher n value obviously have smaller binding energies. When the sample is cooled from room temperature, the exciton lines appear and become finer[21]. Because of this, transmission measurements are usually done at liquid nitrogen or liquid helium temperatures, with even lower temperatures being used for certain measurements. Furthermore, the position of the exciton lines shifts towards higher energy as the temperature is lowered, as does the energy gap (Figure II.3). This shift occurs in such a manner that the energy between exciton lines remains almost constant, as if they were drawn on a template and the template shifted with temperature[23]. At 4.2 K, the experimentally determined positions (in eV) of the P exciton lines of the yellow series are given by[5]

$$E_n^y = 2.17244 - \frac{0.0972}{n^2}$$

following a $1/n^2$ law as predicted. Unfortunately, the S and D exciton lines are less well characterized since they are more difficult to observe. The energy of the exciton transitions at 4.2 K and 77 K are given in Table II.1.

II.5 PHOTOVOLTAIC EFFECT

The photovoltaic cells of interest here are based on a Cu-Cu_2O (metal-semiconductor) junction. Although many metals form what is known as a "Schottky barrier" rectifying contact with Cu_2O, the Cu_2O/Cu junction is the most stable since most other metals tend to reduce Cu_2O to form essentially a Cu_2O/Cu contact.

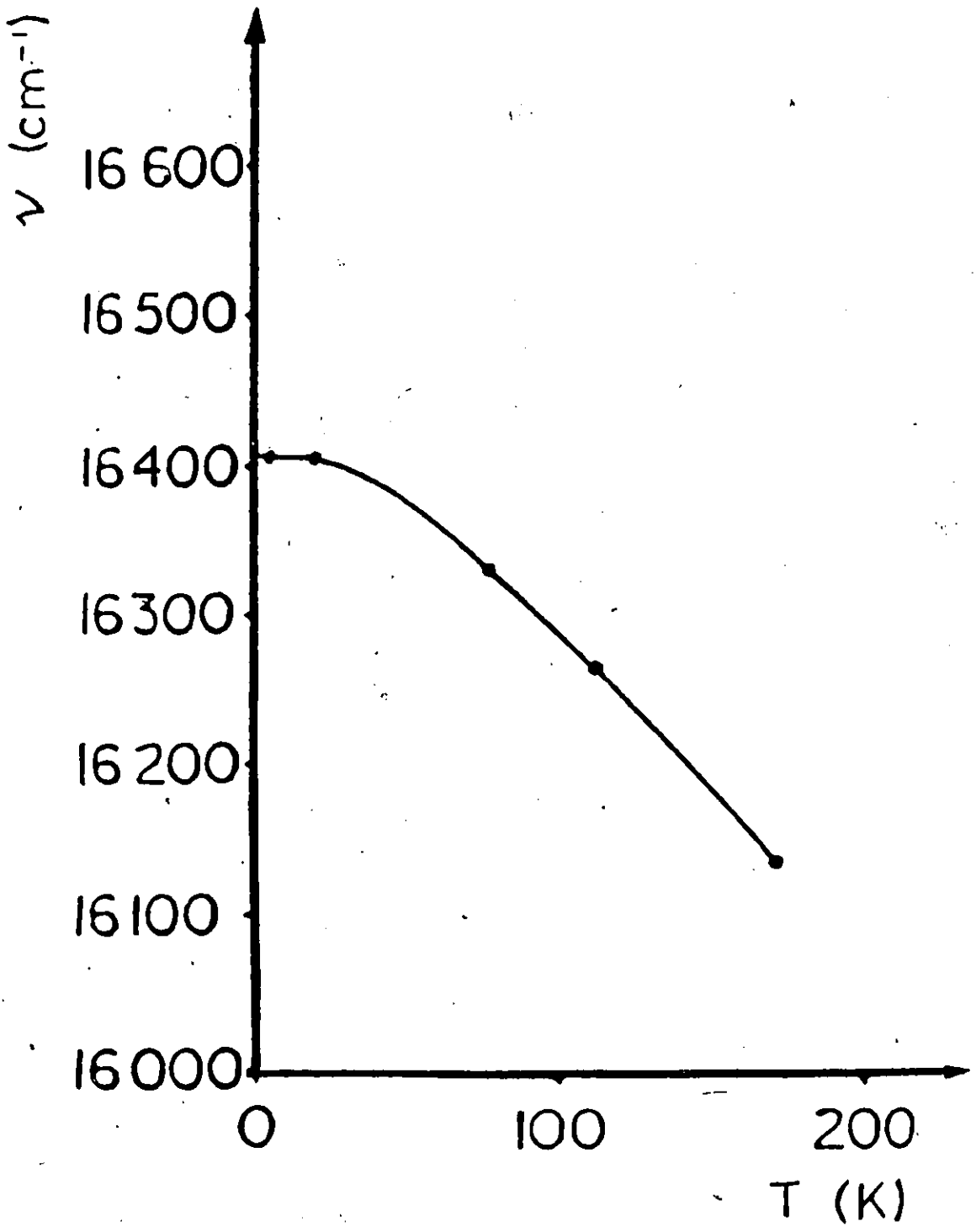

FIGURE II.3 Position of the n=1S exciton line vs temperature [22]

	4.2 K (Ref. 12)			77 K (Ref. 23)	
n	S	P	D	S	P
1	2.0330			2.0234	
2	2.1544	2.1473			2.1396
3	2.1603	2.1609	2.1630		2.1530
4	2.1653	2.1657	2.1666		2.1578

Table II.1
Energies (in eV) of the yellow exciton series levels of Cu_2O in zero field at 4.2 K and 77 K

To understand how a Schottky barrier device functions, the concept of the work function is introduced. When two different materials first make contact, there will be a flow of electrons from one to the other. This is because the electrons meeting the junction from one side will generally have more energy than those meeting it from the other side. Consider a metal M and a p-type semiconductor S, with different Fermi levels W_{FM} and W_{FS}. Before they come into contact, the energies at the surfaces of the metal and semiconductor will be equal and may be taken as zero. It is convenient to consider the energy difference between the Fermi level and the surface, which is known as the *work function*, ϕ. With metals, this is also the depth of the conduction band. If $\phi_M < \phi_S$, on contact there will be an initial flow of electrons from the metal to the semiconductor, so that a positive charge is formed on the metal. The electrons are captured by acceptor atoms near the junction and a depletion layer of width d is formed. The electron flow will proceed until the two Fermi levels coincide. There is then a difference between the surface energy levels of $\phi_S - \phi_M$, and also a potential difference V_{SM} due to the surface charges. With zero external bias, equal and opposite currents I_F and I_0 are set up. The hole current I_F is due to holes from the semiconductor which possess sufficient thermal energy to cross the barrier $\phi_S - \phi_M$ and I_0 is due to holes from the metal crossing the larger barrier $\varsigma - \phi_M$, where ς is the depth of the top of the valence band in the semiconductor. (Figure II.4*a*).

Thus the contact is rectifying and forward bias occurs with the semiconductor positive, which reduces the potential barrier to $\Psi - V$, where $\Psi = \phi_S - \phi_M$ and V is the externally applied potential. (Figure II.4*b*). This allows I_F to increase, while I_0 remains constant since the somewhat larger barrier $\varsigma - \phi_M$ is unaffected by the bias. Reverse bias occurs

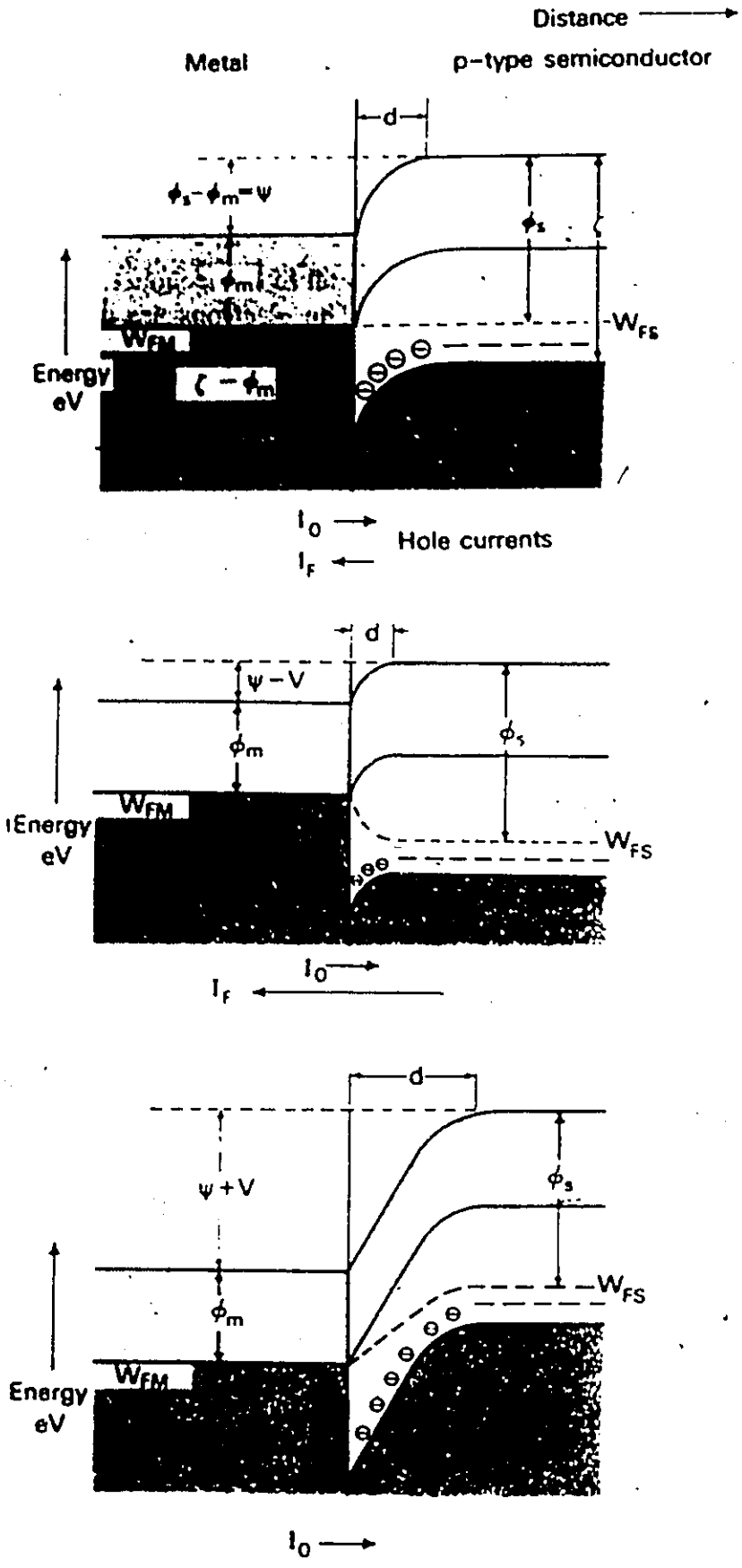

FIGURE II.4 Contact between a metal and p-type semiconductor ($\phi_m < \phi_s$)[41]

a) Energy diagram after contact

b) Energy diagram for forward bias

c) Energy diagram for reverse bias

with the semiconductor negative, which increases the barrier height to $\Psi + V$ so that $I_F \longrightarrow 0$, but I_0 is unaffected (Figure II.4*c*). The width of the barrier also increases with increasing reverse bias. It should be noted that I_0 increases with temperature since it is due to thermally generated carriers.

This system can be used as a photovoltaic detector, with one possible configuration having the light traverse the layer of semiconductor before reaching the metal-semiconductor junction. In such a device there are two charge-creating mechanisms. The first is, as mentioned above, the photoemission of holes from the metal into the semiconductor, in which the threshold photon energy is that corresponding to the barrier height associated with the metal-semiconductor contact[24]. The second mechanism is due to band-to-band absorption of the light by the semiconductor. Should the electron-hole pair be generated in the depletion width or alternatively the electron manage to diffuse to the junction, it results in electron injection from the semiconductor to the metal.

The photocurrent density through the depletion layer due to band-to-band transitions in Cu_2O is given by $J = J_{dl} + J_{diff}$, where J_{dl} is the drift current density due to carriers generated inside the depletion layer, and J_{diff} is the diffusion current density generated outside the depletion layer and diffusing into the reverse-biased junction.

For incident monochromatic radiation, the one-photon absorption and electron-hole generation function is given by

$$g(x) = \Phi \alpha e^{-\alpha x} \tag{11}$$

where $g(x)$ is the generation rate (density generated per unit time), Φ is the incident photon flux, α is the absorption coefficient, and x is the thickness of semiconductor the

photons have traversed, with $x = 0$ being at the surface of the semiconductor. Thus, J_{dl} is found to be

$$J_{dl} = q \int_a^{a+W} g(x) dx \tag{12}$$

where a is the thickness of semiconductor the light must traverse before reaching the junction, and W is the thickness of the depletion layer. This gives that

$$J_{dl} = \left[q\phi(e^{-\alpha W} - 1)\right] \times e^{-\alpha a} \tag{13}$$

Hence J_{dl} drops off exponentially with the thickness of semiconductor the light has to traverse before reaching the depletion width.

To obtain J_{diff}, the diffusion equation

$$D_n n'' - (n - n_0)/\tau + g(x) = 0 \tag{14}$$

must be solved. Here D_n is the diffusion coefficient for electrons, n is the electron density, n_0 is the equilibrium electron density and τ is the lifetime of the electrons. Then, the diffusion current at $x = a + W$ is obtained from

$$J_{diff} = qD_n n' \tag{15}$$

For two-photon absorption, the expressions for J_{dl} and J_{diff} remain the same. However, the generating function will be different. To evaluate it, equation (7) is used as a starting point. Considering only two-photon absorption,

$$\frac{dI}{dx} = -\alpha_2 I^2 \tag{16}$$

Rearranging and integrating gives

$$\frac{1}{I} = \alpha_2 x + c\bar{s}t \tag{17}$$

At $x = 0, I = I_0$, so that

$$I = (\alpha_2 x + 1/I_0)^{-1} \tag{18}$$

Now

$$g(x) = -\frac{1}{h\nu}\frac{dI}{dx} \tag{19}$$

$$g(x) = \frac{\alpha_2}{h\nu} \times \frac{1}{(\alpha_2 x + 1/I_0)^2} \tag{20}$$

$$g(x) = \frac{\alpha_2 I_0^2}{h\nu(\alpha_2 I_0 x + 1)^2} \tag{21}$$

and since $\phi = I/h\nu$,

$$g(x) = \frac{\alpha_2 \phi_0^2 h\nu}{(\alpha_2 h\nu \phi_0 x + 1)^2} \tag{22a}$$

where ϕ_0 is the incident photon flux on the sample. For low absorption, a binomial expansion gives

$$g(x) = \alpha_2 \phi_0^2 h\nu(1 - 2\alpha_2 h\nu\phi_0 x) \tag{22b}$$

Therefore,

$$J_{dl} = q\int_a^{a+W} g(x)dx \tag{23}$$

$$J_{dl} = q\alpha_2\phi_0^2 h\nu \int_a^{a+W} (1 - 2\alpha_2 h\nu\phi_0 x)dx \tag{24}$$

$$J_{dl} = q\alpha_2\phi_0^2 h\nu\left[W - 2\alpha_2 h\nu\phi_0\left((a+W)^2 - a^2\right)\right] \tag{25}$$

$$J_{dl} = q\alpha_2\phi_0^2 h\nu\left[W\left(1 - 2\alpha_2 h\nu\phi_0(2a+W)\right)\right] \tag{26}$$

If W is of the order of (or smaller than) a, then the second term will be much smaller than 1, so that

$$J_{dl} = q\alpha_2\phi_0^2 h\nu W \tag{27}$$

The diffusion equation becomes

$$D_n n'' - (n - n_0)/\tau + \alpha_2 \phi_0^2 h\nu(1 - 2\alpha_2 h\nu \phi_0 x) = 0 \tag{28}$$

which has as a solution

$$n = n_0 - 2x\tau\alpha_2\phi_0^2 h\nu + \tau\alpha_2\phi_0^2 h\nu - C_1 \frac{L_n}{2e^{x/L_n}} + C_2 e^{x/L_n} \tag{29}$$

where C_1 and C_2 can be determined from the boundary conditions:

(i) at $x = a$, $n = 0$

(ii) at $x = 0$, $n = n(0)$,

where $n(0)$ is the electron concentration at the surface of the semiconductor. This gives equation (30):

$$\begin{aligned} n = n_0 &- 2x\tau\alpha_2\phi_0^2 h\nu + \tau\alpha_2\phi_0^2 h\nu \\ &+ \left[\frac{n_0(1 - e^{a/L_n}) + n(0)e^{a/L_n} - 2a\tau\alpha\phi^2 h\nu + \tau\alpha\phi^2 h\nu(1 - e^{a/L_n})}{e^{a/L_n} - e^{-a/L_n}}\right] e^{-x/L_n} \\ &- \left[\frac{n_0(1 - e^{-a/L_n}) + n(0)e^{-a/L_n} - 2a\tau\alpha\phi^2 h\nu + \tau\alpha\phi^2 h\nu(1 - e^{-a/L_n})}{e^{a/L_n} - e^{-a/L_n}}\right] e^{x/L_n} \end{aligned}$$

Now $J_{diff} = qD_n n'$, so that equation (31) is obtained:

$$\begin{aligned} J_{diff} = -\frac{qD_n}{L_n}\Bigg\{ &2\tau\alpha\phi^2 h\nu L_n \\ &+ \left[\frac{n_0(1 - e^{a/L_n}) + n(0)e^{a/L_n} - 2a\tau\alpha\phi^2 h\nu + \tau\alpha\phi^2 h\nu(1 - e^{a/L_n})}{e^{a/L_n} - e^{-a/L_n}}\right] e^{-x/L_n} \\ &+ \left[\frac{n_0(1 - e^{-a/L_n}) + n(0)e^{-a/L_n} - 2a\tau\alpha\phi^2 h\nu + \tau\alpha\phi^2 h\nu(1 - e^{-a/L_n})}{e^{a/L_n} - e^{-a/L_n}}\right] e^{x/L_n}\Bigg\} \end{aligned}$$

The equations in this chapter will be used later on to explain the experimental results from the two-photon photovoltaic effect.

Another important thing to note is that in transmission, the sample is cooled as much as possible so that the exciton lines are as fine as possible. At first the same would

be expected when using the photovoltaic technique. However, this is not the case. At very low temperatures there is not enough thermal (phonon) energy to cause the exciton to dissociate, so that it simply recombines. The problem is that if no electrons reach the conduction band then no photocurrent will be created and no exciton lines detected. Solutions to this problem will be discussed in the next section and in the chapter in which the results are presented and discussed.

II.6 ELECTRIC FIELD EFFECT

The application of an electric field has two distinct effects: one takes place at the Cu_2O/Cu interface, while the other directly affects the excitons. The first of these was introduced in the previous section: a forward or reverse bias will respectively increase or decrease the current I_F crossing the barrier Ψ from the semiconductor into the metal.

The second effect is field ionization of the excitons[25]. This occurs when eEd, the potential energy difference across the diameter d of an orbit, is of the order of magnitude of the binding energy of a particle in orbit. At fields large enough for this to be the case, the lifetime of the state against dissociation becomes quite short, and the line width for absorption to that state becomes correspondingly large. For example, if a depletion width of the order of 5×10^{-8} m is assumed[40], an applied bias of 5 Volts will produce an electric field of approximately 10^8 V/m. This will result in a potential energy difference of 0.1 eV, to be compared with the n=1S exciton's binding energy of 0.14 eV. The effect is thus expected to play a role in observing the exciton lines.

The application of an electric field to the crystal has the added effect of mixing states with different parities, i.e. different values of l. This induces normally forbidden transitions

in the absorption spectrum[5]. Furthermore, it shifts the position of the exciton lines toward longer wavelengths[5].

This brings the chapter to a close. The next chapter will describe the samples to which the theory will eventually be applied.

CHAPTER III SAMPLES

III.1 INTRODUCTION

The various experiments that took place made use of two types of samples. The first consisted of single crystals of copper oxide, and the second type consisted of Cu_2O/Cu Schottky barrier photovoltaic cells. Both types were produced *in situ* using the same basic apparatus. This chapter will contain a description of the oxidation apparatus, followed by a detailed procedure for the production of the samples.

III.2 OXIDATION APPARATUS

All oxidations and annealing required to produce single crystal or photovoltaic effect samples took place in a controlled atmosphere enclosure consisting of a fused quartz tube mounted horizontally. One end of the tube was connected to a high-speed rotary pump with a liquid nitrogen cold trap capable of lowering the pressure of the system to 10^{-5} torr. Also at this end were valves to control the flow of nitrogen and oxygen, the latter being operated either manually or controlled automatically by the electronics associated with a pressure sensor attached to the system. A reservoir in which gases could be stored was also available. The other end of the tube was either sealed or left open, depending on the desired mode of operation. For low pressure operation the sealed end tube was used, and for gas flow the narrow open end was used. From this end, a Lindberg microprocessor controlled furnace could be rolled in to surround the furnace. This was the basic system used to create the samples, be they single crystal or Schottky barrier samples.

The temperature at the center of the furnace was measured directly with a type-K

thermocouple and was found to be slightly higher than the set point temperature of the controller. This difference increased with temperature, reaching roughly 30°C at 900°C (Figure III.1). This difference was found to be of importance in the next section.

III.3 SINGLE CRYSTALS FOR TRANSMISSION

Conventional one and two-photon absorption measurements usually monitor the transmission of a crystal as a function of the incident wavelength of the light. High quality samples are required to achieve good, consistent results. Several techniques[26,27,28,29,30] are available for the production of Cu_2O samples and their preparation for transmission measurements. State of the art crystals are grown by the arc-image technique[30], or by hydrothermal synthesis[31]. Since neither of these systems was available, it was necessary to rely on slightly less sophisticated techniques, where copper is oxidized at various pressures and temperatures.

A problem common to all the methods is that cuprous oxide reacts with most crucible materials[26] including quartz and graphite. To alleviate this problem the copper was mounted on a disposable ceramic support. The support and copper sample were designed so that there was a minimum of contact between the cuprous oxide that eventually formed, and the support. When the oxidation was completed, the sample was delicately separated from the support.

The simplest method of producing Cu_2O samples is the one suggested by Toth, Kilkson and Trivich. It consists in taking high purity copper in the form of sheets between 0.2 mm and 0.9 mm thick. They are cut into any convenient size and etched in nitric acid diluted by de-ionized water in a 1 : 1 ratio. The corners are then bent down 90° to form

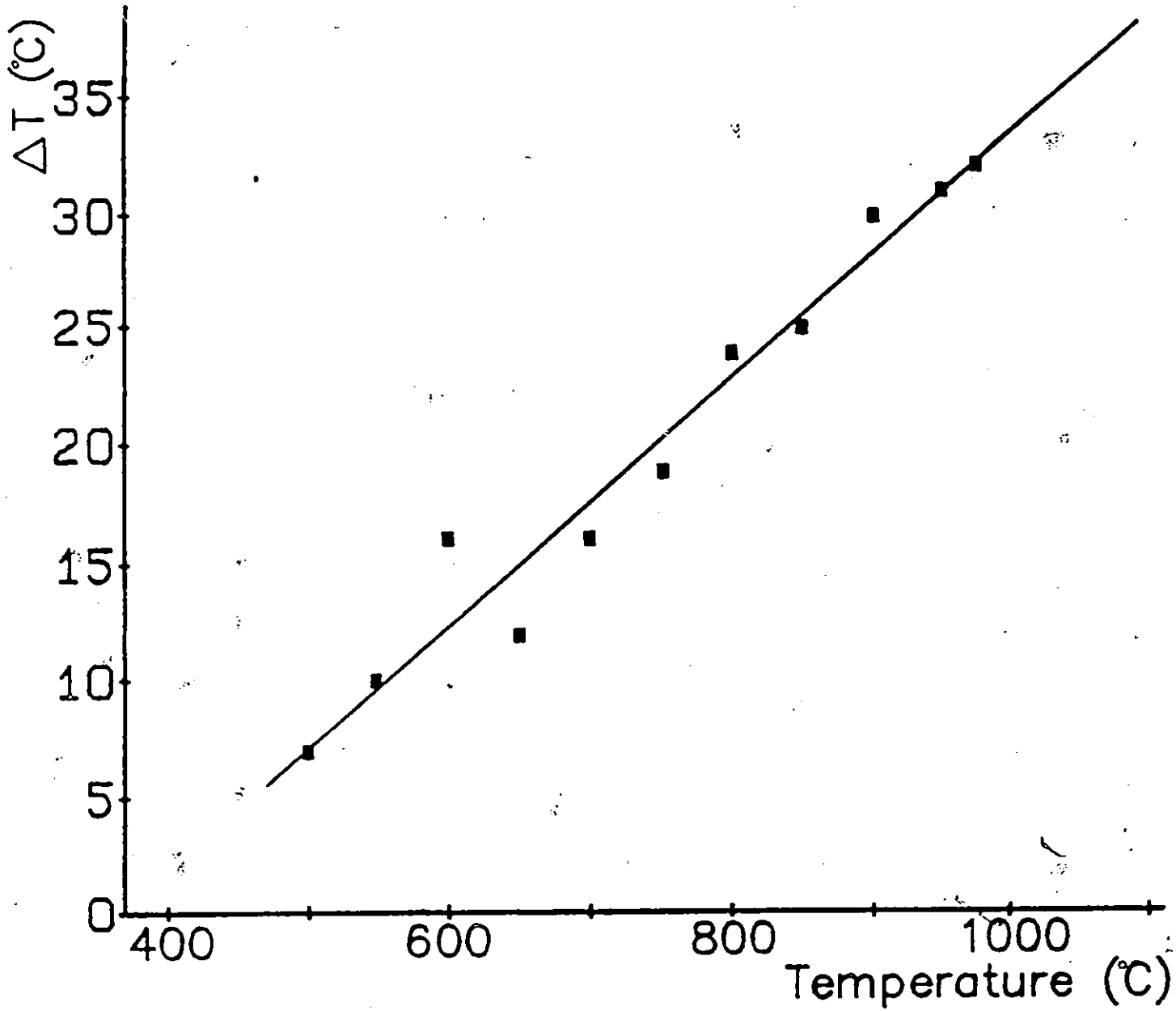

FIGURE III.1 Temperature difference (measured–indicated) vs furnace temperature

small "feet" which are the only points of contact between the copper and the support. This assembly is pushed into the center of the furnace. From the stability diagram for the $Cu/Cu_2O/CuO$ system, Cu_2O is only stable in atmospheric pressure air at temperatures above 1020°C. Since the eutectic point for $Cu\text{-}Cu_2O$ is at 1065°C, it is necessary to oxidize at a temperature between these two points (Figure III.2). After the oxidation is completed, the temperature is raised to a value between 1085°C and 1130°C, depending on the thickness of the plate. The polycrystalline samples are then allowed to anneal at these temperatures for times ranging between 5 to 150 hours, to allow secondary recrystallization to occur. After the annealing is over, the samples are quenched by quick withdrawal from the furnace. The thin layer of cupric oxide (CuO) formed during this step is removed by etching in dilute HNO_3 or by the use of abrasives.

A handful of attempts at producing single crystal samples using this technique were made. The result in all cases was that when the temperature of the sample was raised for annealing, the feet collapsed and/or reacted with the support so that the whole Cu_2O sample came into contact with the support, reacted with it, and became unuseable. The probable cause of this was the higher than indicated temperature at the center of the furnace, bringing the sample too close to the Cu_2O melting point for it to support its own weight. This technique was not reattempted because the following technique, giving better results, was discovered.

This technique, developed by Ebisuzaki[28], was used to produce all the Cu_2O samples used for transmission measurements. The method was used to prepare thick single crystals of Cu_2O of large surface area. A piece of monocrystalline copper was required for the

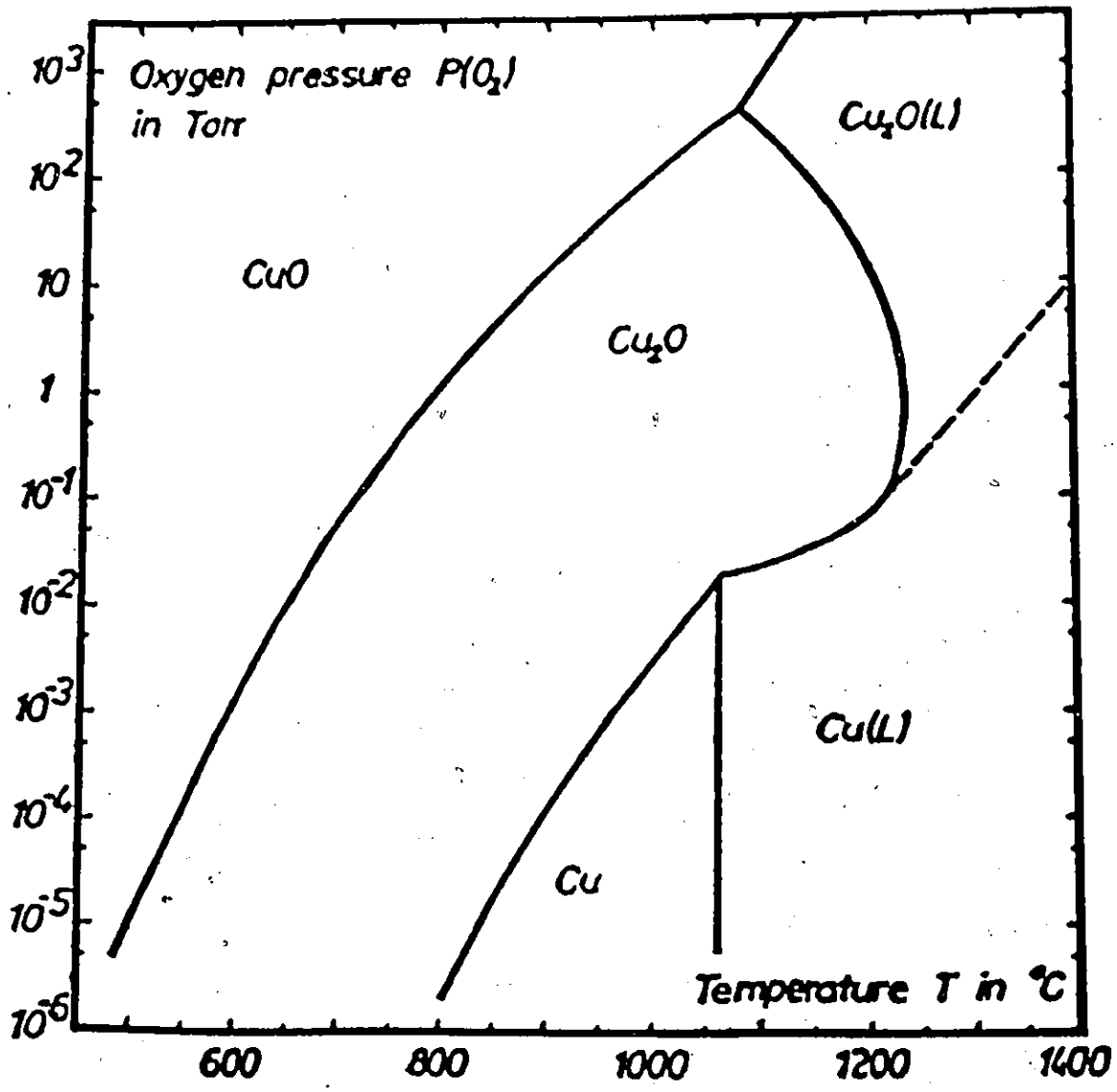

FIGURE III.2 Pressure vs temperature diagram in the copper-oxygen system[42]

oxidation. Small cylindrical copper samples 8 mm in diameter by 30 mm long were grown using the Bridgman technique[32]. Slices of 1.5 mm to 3 mm thickness were cut from the rod. They were mechanically polished to a mirror finish using polishing alumina down to 1 μm. Some of the samples were then electrolytically polished in orthophosphoric acid[33]. Since single crystals were also obtained without electropolishing, this step was later dropped. The samples were then rinsed in de-ionized water.

The technique then required that the sample be oxidized under low oxygen pressures provided, in Ebisuzaki's case, by the impurities of about 0.2% oxygen in tank nitrogen, increased eventually to a flowing mixture of 3.1 mm Hg of oxygen and tank nitrogen for several days. To suit the available equipment, the technique was modified slightly. A cylinder of ultra-high purity nitrogen and a separate oxygen cylinder were connected to one end of a quartz tube, with the other end left open. At room temperature, the oxygen valve was adjusted so that an increase of 0.2 torr in 10 seconds occured if the open end was blocked. Similarly, the nitrogen valve was adjusted to yield an increase of 50 torr in 5 seconds. For some samples only nitrogen flowed through the tube when the furnace was first turned on. Once the oxidation temperature of 980°C was reached, oxygen was allowed to flow through the system. For other samples, oxygen flowed with the nitrogen from the start. No discernable difference between the resulting samples was found. Cooling was done with only nitrogen flowing.

By this method copper disks of 1.5 mm thickness were converted into Cu_2O crystals approximately 2.5 mm thick. The resulting Cu_2O crystals had slightly rounded surfaces and a region of voids (or remaining copper if not oxidized for a long enough period of time)

in the central region corresponding to the central plane of the original metal. The crystals were cut through this central region and both sides of each slice were polished, again using polishing alumina down to 1 μm. The cuprous oxide crystals thus obtained had smooth, shiny surfaces and a dark bluish color when held against an opaque background. When held up to a light source, they were a translucent red color.

Laue reflection photographs of several samples showed them to be single crystals. Other samples had two distinct crystals while samples that were oxidized at too high an oxygen pressure were polycrystalline. Attempts were made to anneal the polycrystalline samples to increase the grain size. The samples were annealed at a temperature of 1000°C at oxygen pressures ranging from 0.02 torr to 10 torrs and for times ranging from 12 to 64 hours. The results were slightly disappointing: although the grain size grew slightly, the Cu_2O had been transformed back into copper. Later it was discovered that this was only a surface effect. Dipping the sample in nitric acid, rinsing it in de-ionized water and then wiping it off on lint-free paper removed the copper layer, exposing the Cu_2O underneath.

III.4 PHOTOVOLTAIC EFFECT SAMPLES

Samples grown specifically for use by the photovoltaic effect were simpler, faster and more reliably produced than their counterparts used for transmission measurements. Although the last difference may be attributed to the much greater amount of research done in the department on this type of samples, the first two were due to fundamental differences in the techniques: one required single crystal copper and days to oxidize, the other, industrial grade copper and seconds to oxidize.

The photovoltaic effect samples consisted of a thin layer of cuprous oxide grown thermally on a copper substrate. Industrial grade copper sheets of 1 mm thickness were cut into squares 1 cm by 1 cm. They were cleaned in nitric acid diluted by de-ionized water in a 1 : 1 ratio and then rinsed in de-ionized water. This was followed by the usual polishing using aluminium oxide powder. This polishing step was more important for the growth of thin ($< 20\ \mu m$) Cu_2O layers, since surface irregularities in the copper substrate could lead to pin holes in the oxide and hence to shorting paths in the sample. Only one side of the copper was polished since only one face of the resulting photovoltaic cell was studied.

The copper was then mounted vertically in a notch cut into a ceramic holder and inserted into the quartz tube for oxidation. The system was evacuated to at least 10^{-4} torr. Then, 100 torr of oxygen was let into the system, including the reservoir. The reservoir was then sealed and the rest of the system re-evacuated. The sample would later be exposed to the oxygen in the reservoir to produce Cu_2O. While this was taking place, the furnace was pre-heated to 1000°C. When the system had achieved its minimum pressure, the furnace was rolled in around the quartz tube. The temperature reading of the furnace was allowed to restabilize at its initial value. At this point the valve between the pump and the system was closed and the reservoir valve opened for times ranging from 5 seconds to 2 minutes, depending on the thickness of oxide desired. The reservoir valve was then closed and the pump valve opened. The system pressure was monitored until it reached 10^{-2} torr, which usually took less than 30 seconds. At that point the furnace was removed and a fan turned on to cool the quartz tube. The pumping system was left on so that cooling took place under vacuum, assuring that no CuO could be formed.

After cooling for an hour, the system could be opened and the samples removed. At this point, thin samples had a reddish tint through which underlying copper crystallites could be seen. Thicker samples were a deeper red and the copper was less visible. No polishing of the oxide layer was required, its surface being very smooth. The quality of the oxide layer depended very much on how well the initial copper had been prepared.

The samples were then transfered to a Veeco Model 7710 cryo-pumped evaporator system where an 80 Å semitransparent gold layer was evaporated onto the center of the sample (Figure III.3). Gold was used because it forms an ohmic (non-rectifying) contact[34] with cuprous oxide since its work function is higher than that of Cu_2O. This served as the front electrode for the sample. The back electrode was simply the copper substrate. To gain access to the copper, the oxide was delicately scraped away on one of the corners of the sample. Care was taken not to scratch the thin oxide layer where the gold had been evaporated since this would have resulted in a short-circuited cell. Wires were connected to the electrodes using silver print, making sure once again that the same drop of silver print did not come into contact with both electrodes.

Problems were often encountered with these contacts when the samples were cooled for an experiment. The wires would frequently come off, ending the experiment prematurely. This was especially noted in cryostats using a cold finger. The grip of the silver print was improved by placing a drop of it on a piece of paper for a few minutes. When some of the solvent had evaporated and the drop become tacky, it was applied to the contact. Cryostats using an exchange gas suffered less from contact problems, presumably because the cooling was more gradual.

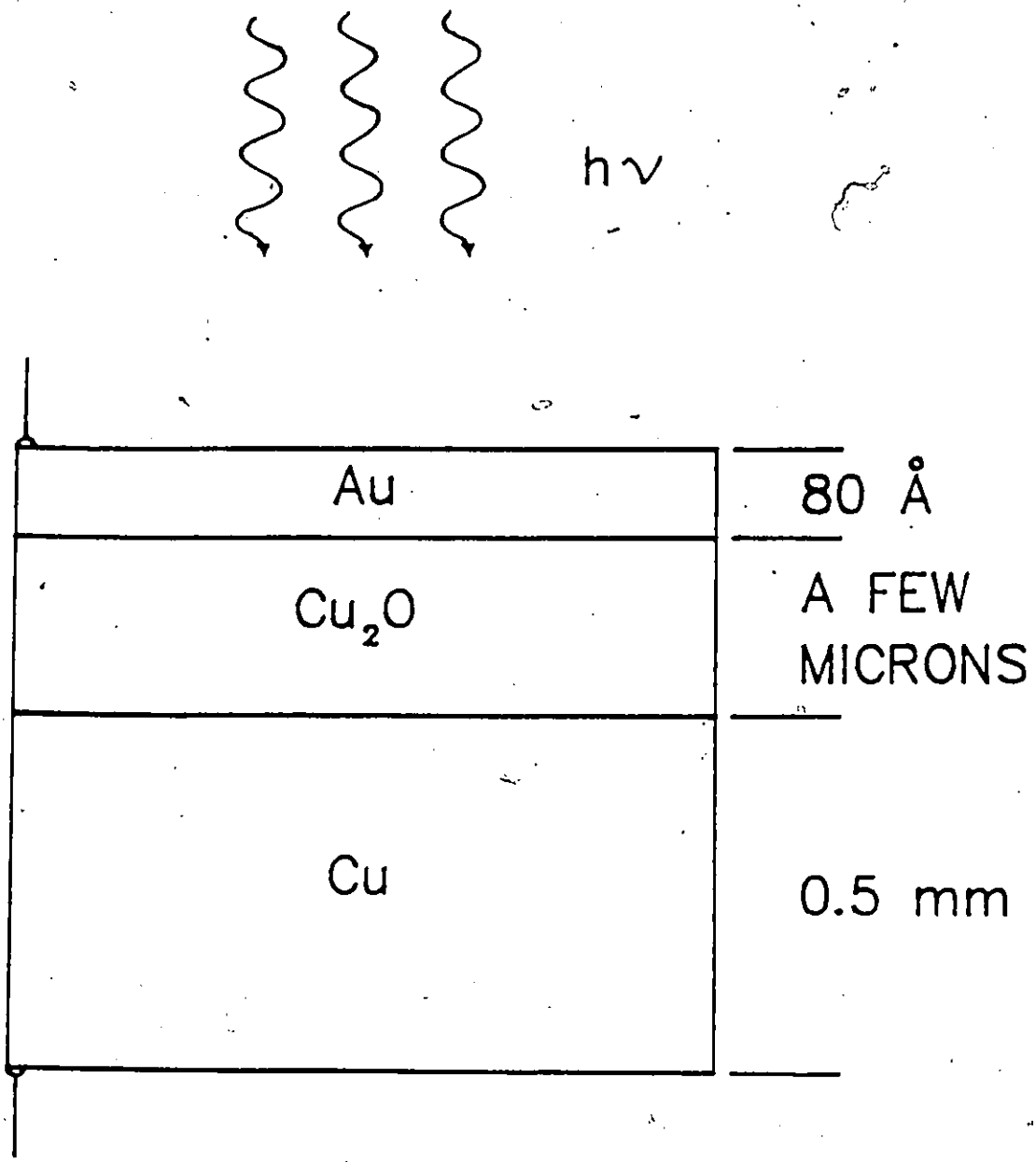

FIGURE III.3 Photovoltaic effect sample

CHAPTER IV EXPERIMENTAL SET-UP

IV.1 INTRODUCTION

This chapter introduces the equipment utilized during the experiments. A wide range of equipment will be described, beginning with the cryostats used to cool the samples to cryogenic temperatures, followed by sections describing the apparatus used in the low and high-intensity experiments.

IV.2 CRYOSTATS

Cryostats with optical access were required since most of the optical measurements were performed at low temperatures. Several cryostats were used during the course of the study. The simplest one, made by Andonian Associates, Inc., proved to be very reliable. It was a cold finger cryostat equipped with a radiation shield between the cold finger and outer wall. This shield was in thermal contact with the cryogenic liquid and/or its vapour, so that the cold finger was insulated from the room temperature radiation. When used with liquid nitrogen (T= 77.3 K), copper-constantan thermocouple readings at the end of the cold finger indicated a temperature of 78.3 ± 0.5 K. Note that for the greatest accuracy, the reference junction was kept at a temperature as close as possible to the temperature to be measured. For most measurements, it was kept in a liquid nitrogen bath. When liquid helium was transferred into the cryostat, thermocouple readings indicated a cold finger temperature of roughly 25 K. This cryostat was equipped with two windows so that it could be used for transmission measurements as well as for photovoltaic measurements. It was found to be ideal for measurements close to liquid nitrogen temperature.

The second cryostat consisted of a bulky unit 60 cm high by 15 cm in diameter (Figure IV.1). Surrounding the sample area was a superconducting magnet. The cryostat was provided with an area between the inner reservoir and outer wall where liquid nitrogen could be poured in to protect the inner liquid. A heater was constructed and installed in the sample area (Figure IV.2). It was mounted on teflon washers and surrounded by a teflon cylinder to insulate it from the rest of the cryostat. This allowed the sample temperature to be varied continuously. A copper-constantan thermocouple was mounted with one junction in liquid nitrogen and the other on the outside edge of the cylinder to monitor the temperature. Another copper-constantan thermocouple was used to monitor the temperature of the heater and sample. An additional technique, consisting of monitoring the forward voltage required to keep a constant current flowing through a diode, was used[35] in parallel with the thermocouple to measure the heater temperature. The linear variation of the voltage with temperature made it ideal for monitoring the temperature. A Litton 209 diode was calibrated from room temperature to 50 K with 1 mA of current flowing through it (see Appendix A for calibration curve). Since the current would heat up the diode, the power supply would only be switched on long enough to measure the voltage. Readings were taken before and after a scan to avoid introducing noise on the photovoltaic signal. Because of the wires required for the heater and to measure the temperature, optical access was limited to one end. Therefore the cryostat could only be used for photovoltaic effect experiments.

The third cryostat consisted of a system by Oxford Instruments that comprised a CF204 cryostat and a DTC-2 temperature controller (Figure IV.3 and Figure IV.4). The

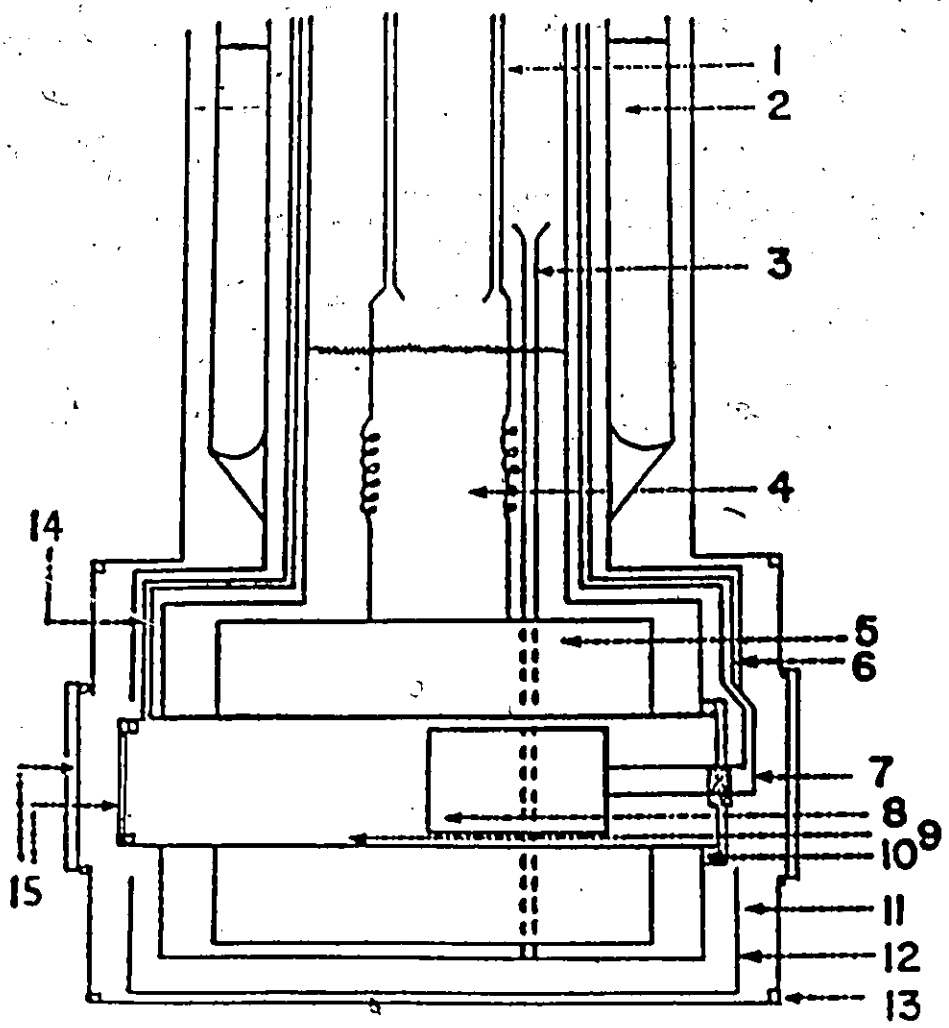

1. Helium recovery tubes and electrical contacts for magnet
2. Liquid nitrogen
3. Guide for helium transfer line
4. Liquid helium
5. Superconducting magnet
6. Wires for sample
7. Rear plate and feed-through for wires
8. Heater surrounded by teflon sleeve
9. Sample chamber
10. Indium seals
11. Vacuum chamber
12. Copper heat shield
13. O-ring seal
14. Tube for helium exchange gas
15. Windows

FIGURE IV.1 Diagram of cryostat containing superconducting magnet[17]

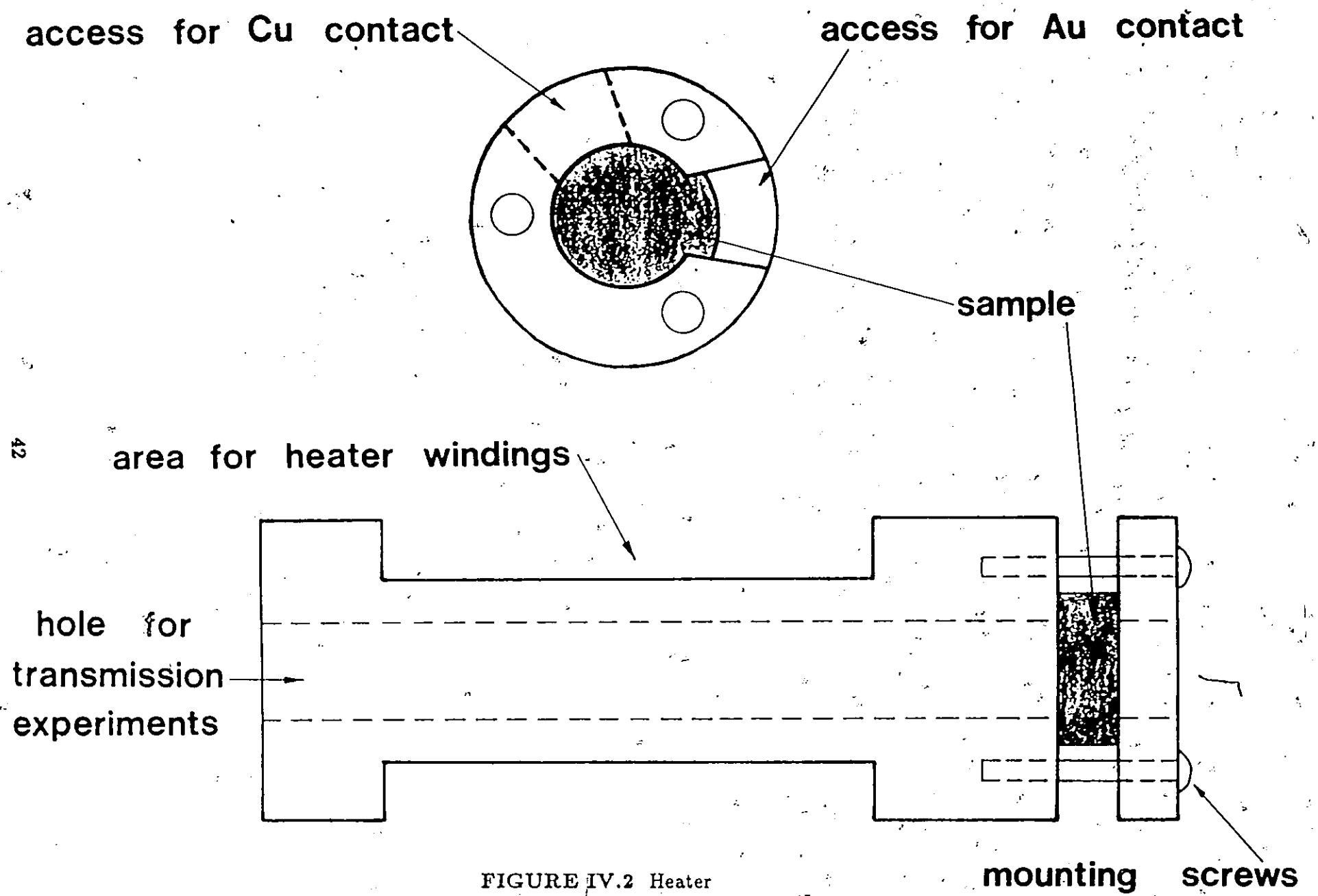

FIGURE IV.2 Heater

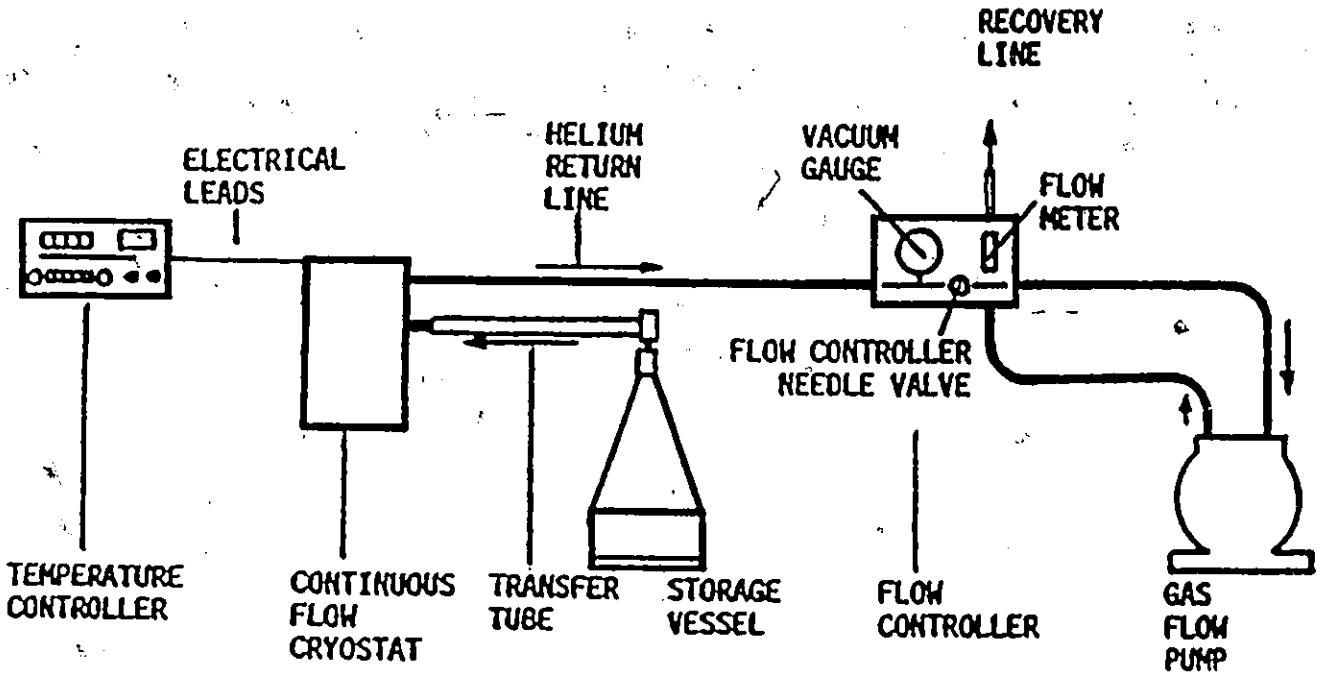

FIGURE IV.3 Diagram of Oxford Instruments system [43]

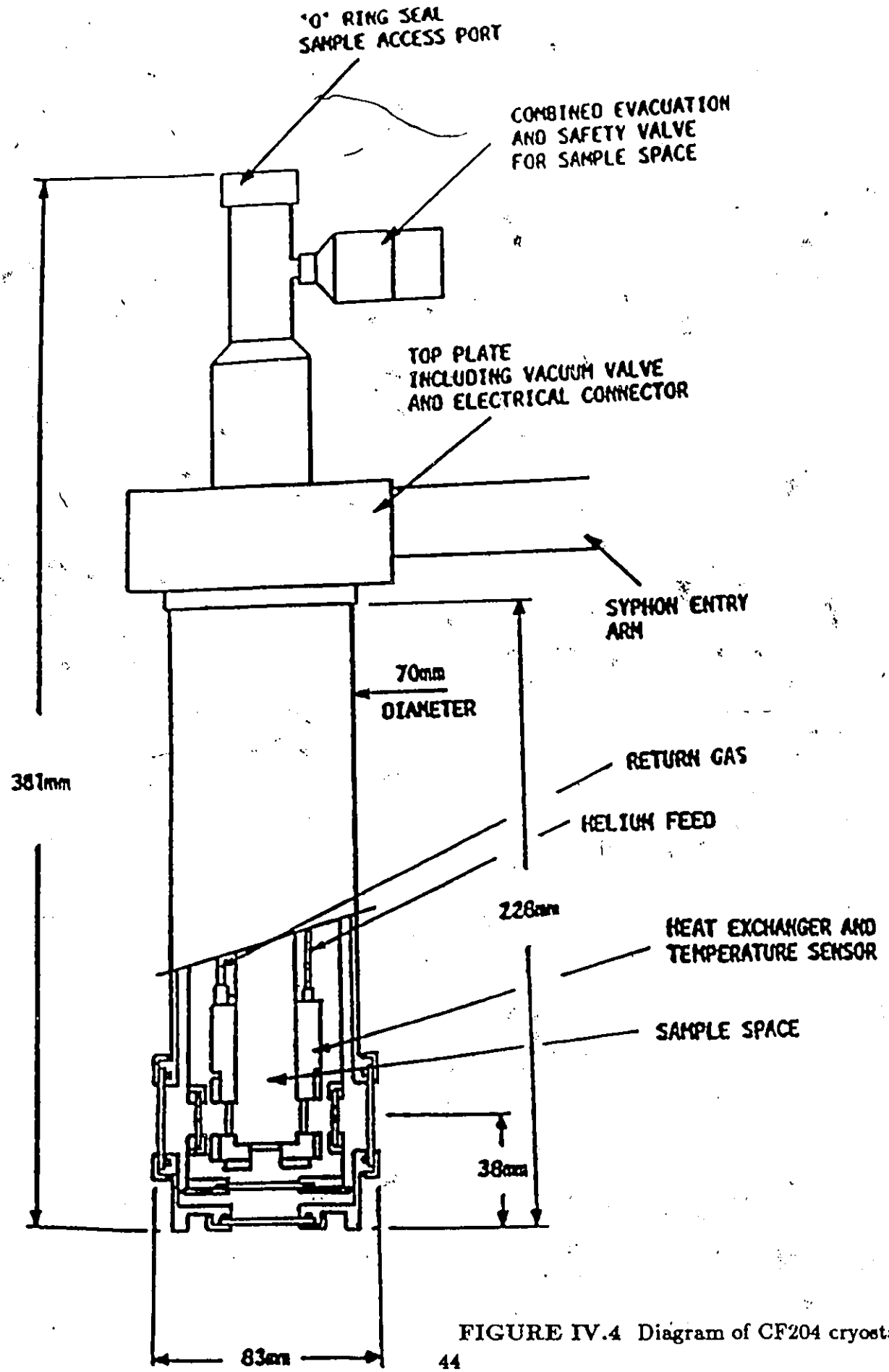

FIGURE IV.4 Diagram of CF204 cryostat[43]

cryostat was connected via a special transfer line to a helium or nitrogen tank. A diaphragm pump connected to the cryostat pulled the liquid from the tank and into the cryostat. The liquid helium (or nitrogen) flow was regulated by the temperature controller. Typical flow rates of under 0.5 litres of helium per hour were noted at a steady state temperature of 77 K. The sample chamber's temperature could also be regulated automatically by a heater and thermocouple connected to the temperature controller. Optical access was provided by 5 ports, all at 90° to each other. The samples were mounted on the end of a stainless steel rod that descended into the sample space. A helium exchange gas was used to cool the sample. A gold-plated radiation shield was located between the sample chamber and the outer wall. This was the cryostat that was used for all of the infrared measurements and some of the measurements in the visible. The transmission of the windows was measured and found to be without structure in the wavelength ranges of interest. The only drawback to this cryostat was that it had to remain attached to the cryogenic liquid reservoir for the duration of the experiment. However, its small dimensions, reliability and optical accessibility more than made up for this minor inconvenience.

IV.3 LOW-INTENSITY APPARATUS

Many low intensity measurements were performed before attempting to use the parametric oscillator. All of these measurements were performed using a 3/4 meter Spex spectrometer. For all of the measurements in the visible a 600 grooves/mm grating blazed at 7500 Å was used, providing a dispersion of about 20 Å/mm at 6000 Å. Most of the time it was operated with a slit width of 200 μm or less. It was also used for most of the measurements performed at 1.15 μm. Another grating, with 300 grooves/mm was used

for the rest of the measurements in the infrared. The spectrometer was calibrated and frequently monitored with a helium-neon laser to insure accurate wavelength calibration.

Early measurements in the visible were done with a tungsten lamp as the spectrometer's light source. A special current stabilized power supply was constructed for use with it. To increase intensity without sacrificing resolution, a high-pressure xenon arc lamp was used for the rest of the low intensity measurements. A high-pressure mercury lamp was also available but was not used since its spectrum displayed a doublet in the region where the exciton lines were expected. Finally, the light leaving the spectrometer was focussed onto the sample to maximize the resulting signal.

When measuring the reference intensity or the transmission of the samples at low intensities, two detectors were employed. In the visible, an Ealing 28-7821 photovoltaic cell with a sensitivity control spanning 6 orders of magnitude of photocell current was used. A voltage proportional to the photocell current was available at an output socket and used to monitor all measurements. A J-12LD detector, made by Judson Infrared, Inc., was used for low intensity infrared measurements. The low-intensity measurements were performed with the use of a chopper so that a lock-in amplifier and its associated improvement in the signal-to-noise ratio could be used. Because of the high photovoltaic effect sample impedance at low temperatures, a high input impedance lock-in was required to properly match the recording system to the detector. Ultimately, a Stanford Research Systems SR510 lock-in amplifier with a 100 MΩ input impedance was used.

The output from the lock-in was transfered to a Nicolet Instrument Corporation NIC1170 digital storage oscilloscope for most of the low intensity measurements on Cu_2O.

From there, it could be displayed and selected regions amplified before plotting it on a chart recorder. For the rest of the measurements, the output of the detection electronics was sent to an ADALAB analog/digital/analog converter connected to an APPLE computer, where the data could be stored on disk. From there it could be recalled and displayed on the monitor, selected areas expanded, compared with other curves and plotted. Mathematical manipulations including operations such as normalizing the area under two curves, were possible with this system.

A circuit capable of applying a variable bias voltage to the photovoltaic samples was constructed (Figure IV.5). This circuit would be of use for the low and high intensity measurements at infrared wavelengths. The capacitor was added to cut out the D.C. component of the signal and avoid overloading the lock-in amplifier.

IV.4 APPARATUS FOR HIGH-INTENSITY MEASUREMENTS[36]

Most two-photon experiments are done using a fixed wavelength laser as one source and using a low intensity variable wavelength source to scan across the range of interest. Using a variable wavelength laser makes it possible to simplify this to one source emitting photons of half the energy required for the desired transition. The problem arises in finding a tunable pulsed laser that emits in the required wavelength range. At 77 K, Cu_2O has an energy gap of 2.17 eV, half of this being about 1.08 eV. This corresponds to a wavelength of about 1.15 μm. The CMX-4/IR, a parametric oscillator containing a lithium niobate $LiNbO_3$ crystal in an optically resonant cavity pumped by a CMX-4 tunable pulsed dye laser can be tuned to emit in this region.

The principle of operation is based on the second order response which by symmetry

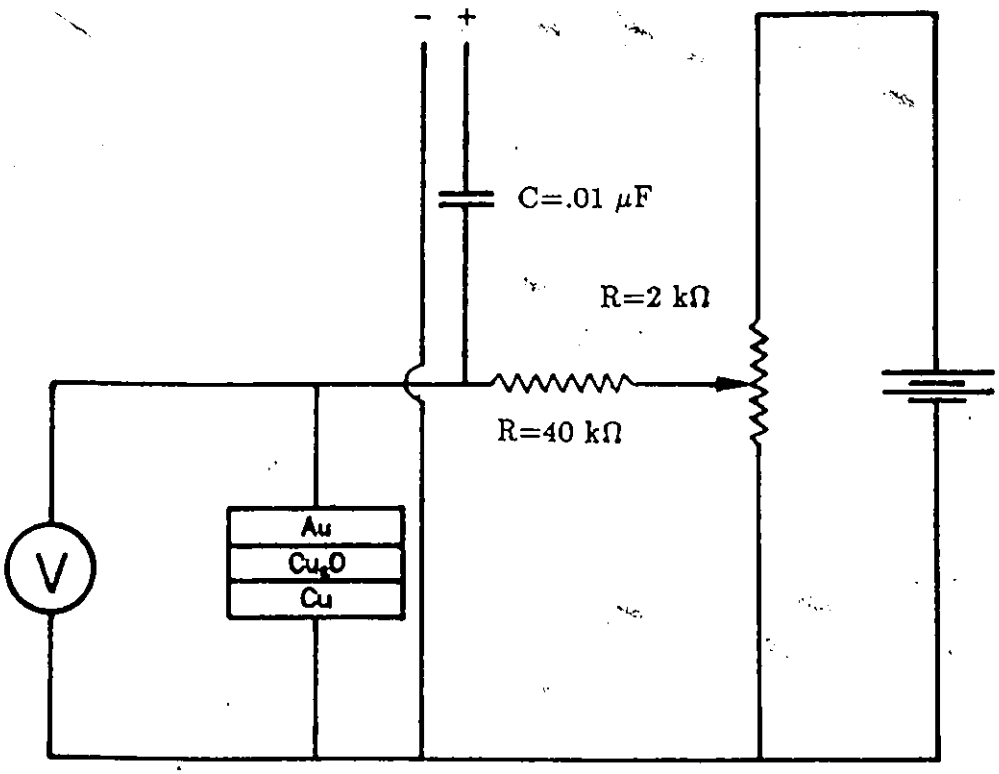

FIGURE IV.5 Schematic of variable bias circuit

arguments occurs in noncentrosymmetric crystals such as $LiNbO_3$. Three different frequencies are involved: the pumping frequency (ν_p), and the two frequencies generated in the crystal, one called the signal (ν_s) and the other, the idler (ν_i). A visible pumping beam incident on the $LiNbO_3$ crystal initiates spontaneous emission or parametric fluorescence of signal and idler photons. Through the non-linearity of the $LiNbO_3$ crystal, spontaneously emitted signal electric fields mix with the pumping field to generate an idler field. This idler field mixes with the pumping field to generate a larger signal field. The process continues with exponential growth at both the signal and idler frequencies[37].

Tuning is achieved by varying the crystal birefringence while simultaneously satisfying the frequency and phase-matching conditions:

$$\nu_p = \nu_s + \nu_i \tag{32}$$

and

$$k_p = k_s + k_i \tag{33}$$

The frequency and phase matching equations are solved for signal and idler frequencies at a given temperature and pump frequency as a function of the tuning variable, which in this case is the pumping frequency. To carry out the calculation, the indices of refraction must be given by an analytical expression. For $LiNbO_3$, the equations are given by:

$$n_o^2 = 4.9130 + \frac{1.173 \times 10^5 + 1.65 \times 10^{-2} T^2}{\lambda^2 - (2.12 \times 10^2 + 2.7 \times 10^{-5} T^2)^2} - 2.78 \times 10^{-8} \lambda^2 \tag{34}$$

for the ordinary ray and

$$n_e^2 = 4.5567 + 2.605 \times 10^{-7} T^2 + \frac{0.970 \times 10^5 + 2.70 \times 10^{-2} T^2}{\lambda^2 - (2.01 \times 10^2 + 5.4 \times 10^{-5} T^2)^2} - 2.24 \times 10^{-8} \lambda^2 \tag{35}$$

for the extraordinary ray, where T is the temperature in degrees Kelvin and λ is the wavelength in nanometers[38]. These dispersion curves are the same for every $LiNbO_3$ crystal except for the fact that there is a temperature shift from one crystal to another. In $LiNbO_3$, the extraordinary pumping ray is transformed into the two infrared ordinary rays. Phase matching with the pump beam polarized along the extraordinary axis and the I.R. beams polarized along the ordinary axis is the simplest case. Under these conditions, the phase-matching equation becomes:

$$n_e(\nu_p)\nu_p = n_o(\nu_s)\nu_s + n_o(\nu_i)\nu_i \tag{36}$$

Analytical techniques can then be used to solve for the signal and idler frequencies as a function of the pumping frequency at fixed crystal temperatures.

It is possible to operate the parametric oscillator in two modes. Although the doubly resonant oscillator (DRO) requires less pumping to achieve threshold, it suffers from the disadvantage of requiring simultaneous resonance at the signal and idler frequencies within a single cavity. This double resonance leads to amplitude and frequency instabilities. This is why operation as a singly resonant oscillator (SRO) is used whenever possible. In this configuration, the idler wave is resonant, and the signal wavelength is free to adjust so that $\nu_p = \nu_s + \nu_i$ is satisfied as the pumping wavelength is varied.

The CMX-4/IR is accompanied by curves of the IR output wavelength versus the pump wavelength (Figure IV.6 solid lines). Unfortunately, they only span the range covered by Rhodamine 6G. The linewidth of the IR output can be determined from Figure IV.7, a graph of the output linewidth versus a parameter δ defined by

$$\delta = \frac{2\lambda_p - \lambda_s}{\lambda_s} \tag{37}$$

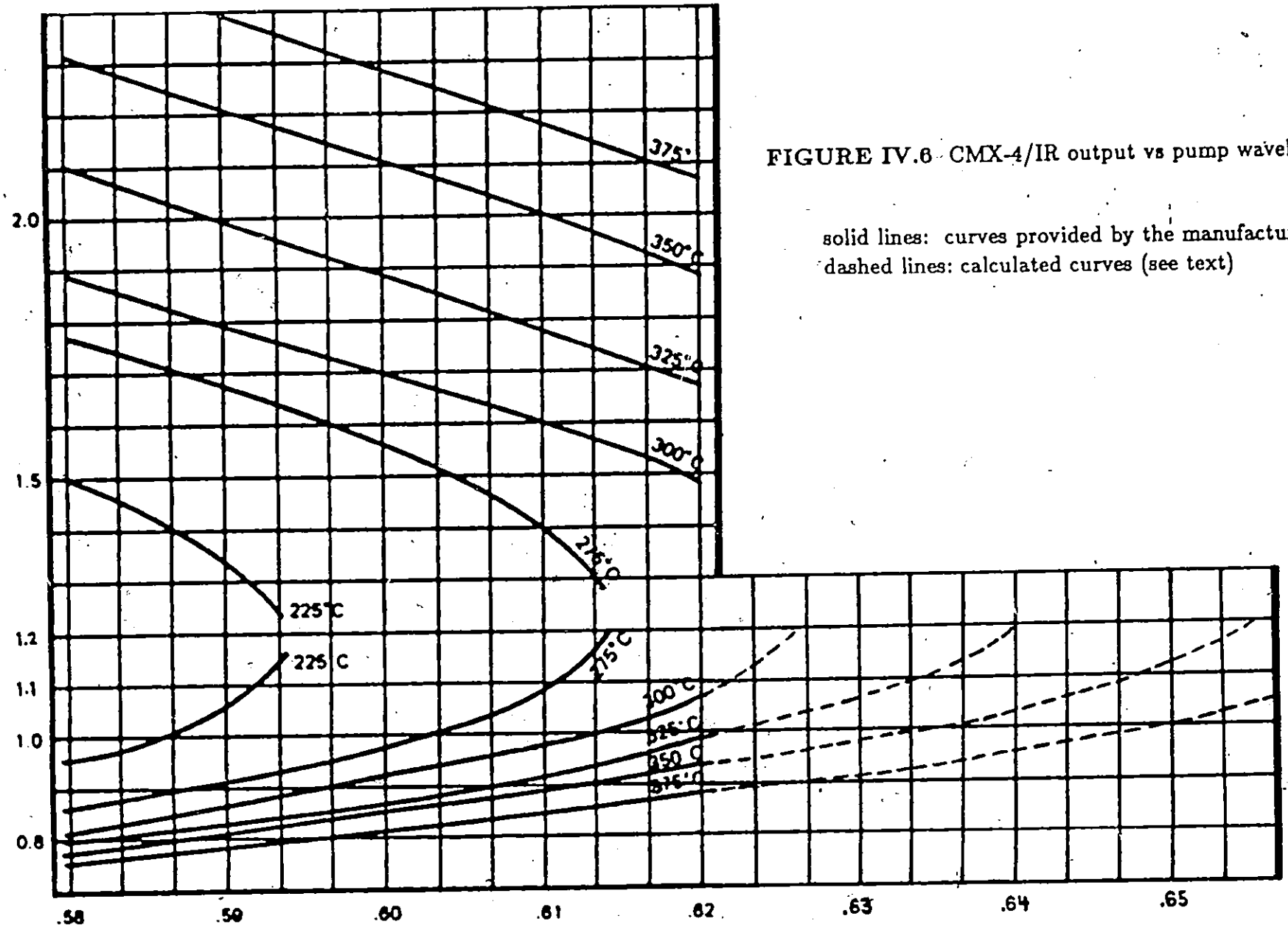

FIGURE IV.6 CMX-4/IR output vs pump wavelength[37]

solid lines: curves provided by the manufacturer
dashed lines: calculated curves (see text)

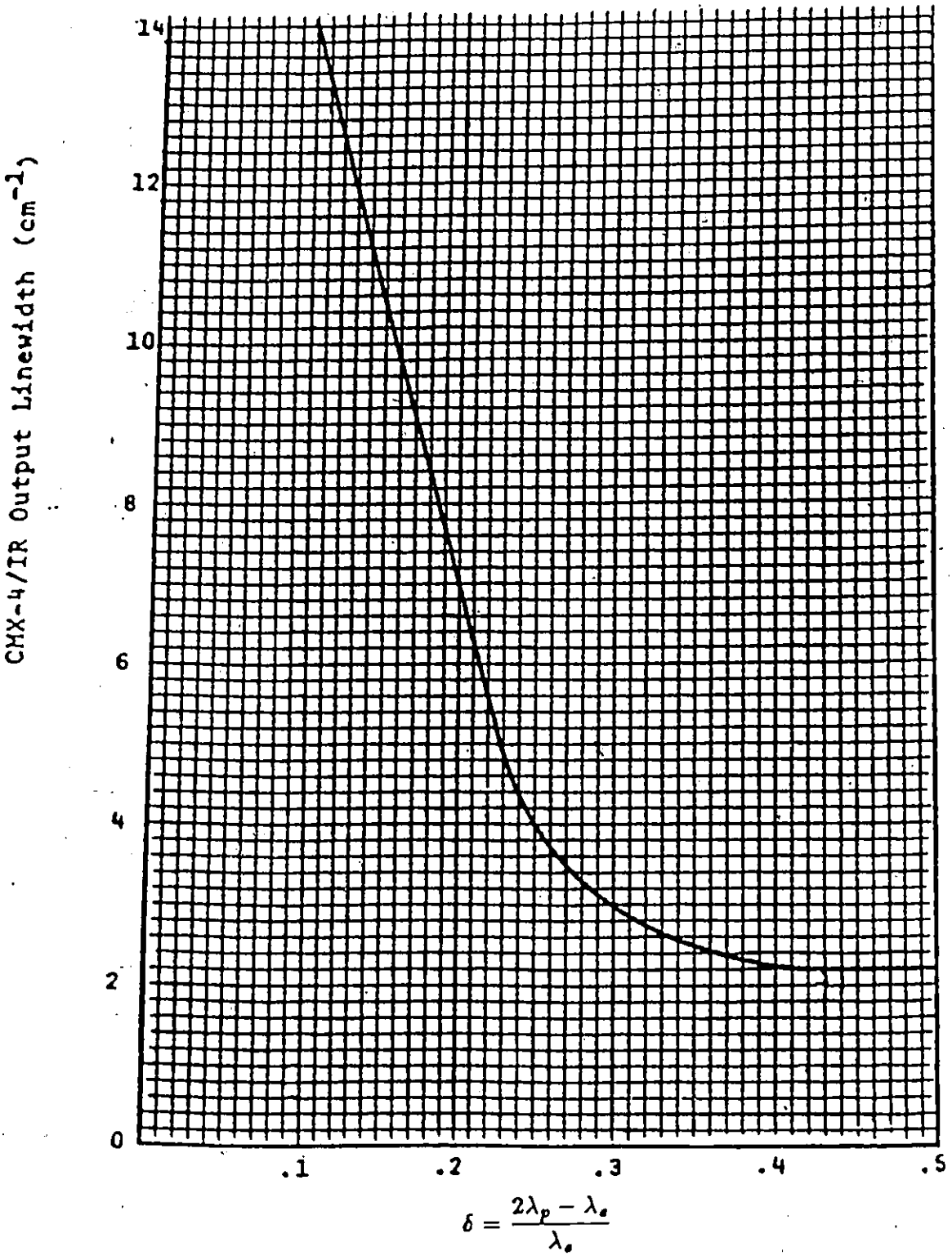

FIGURE IV.7 Linewidth of infrared output vs parameter δ [37]

As luck would have it, pumping with R6G would have lead to an unacceptable IR linewidth in the range of concern ($\simeq 1.15\mu$m), so that the parametric oscillator had to be recalibrated using the analytical technique described previously. Rhodamine 640 was selected as a pumping dye because of its long lifetime while in use. Dyes emitting at even longer wavelengths were not used because of their short duty cycles and because excessive $LiNbO_3$ crystal temperatures would have been required. Furthermore, preliminary research in the early 1970's failed to discover nonlinear absorption in $LiNbO_3$ at wavelengths greater than 0.66 μm. Under the revised operating conditions, the linewidth of the laser was found to be approximately 10 cm^{-1}, or slightly greater than 0.001 eV. This linewidth, though marginal, was thought to be sufficient to resolve the exciton lines of the yellow exciton series.

Apart from the change in dyes, the transmission characteristics of the available mirrors for the parametric oscillator were measured. They were selected to be reflecting at the idler frequency and highly transmitting at the signal and pump frequencies. The gain and output are larger when both mirrors are highly reflecting at the idler frequency. Furthermore, all of the output occurs at the signal frequency. Two mirrors referred to as IR1 by the manufacturer were used since they satisfied the above conditions.

The instructions for the alignment of the parametric oscillator were then followed to the letter. A lot of time and patience was required during this step because the slightest misalignment was enough to prevent the oscillator from functioning.

Since the pumping power was limited by the dye being used, the temperature of the $LiNbO_3$ crystal was set at 370°C as determined by the analytical calculations, so that

the desired infrared wavelength was produced by pumping at the peak power wavelength of the dye laser. To verify that the calibration of the parametric oscillator was accurate, the pumping and infrared wavelengths were measured with the spectrometer for several pumping wavelengths. Slight shifts in infrared wavelength due to differences between one crystal and the next, as mentioned previously, could then be corrected for on the calibration curves (Figure IV.6 dashed lines). From this point on, the pumping laser was controlled using the automatic scanning accessory to insure the accuracy and reproducibility of the pumping wavelength.

A filter was then installed in the beam path at the exit of the parametric oscillator to eliminate the light at the unwanted pump wavelength and the resulting infrared power versus pumping wavelength measured using a pyroelectric detector (Figure IV.8). Its peaked distribution was characteristic of the intensity from the pumping laser. Using a Scientech 361 power meter, the average infrared power at 10 pulses per second was measured to be 1 mW at the peak in the distribution. If a focussed beam diameter of 1 mm and a pulse width of 1 microsecond are assumed, this leads to a peak intensity of 3 kW/cm^2.

The output from the sample was connected to a preamplifier and then to a Princeton Applied Research Model 162 boxcar averager. The output of the boxcar was connected to the ADALAB system where it was recorded on diskettes for further analysis. The experimental setup for the high intensity measurements is shown in simplified form in Figure IV.9.

Now that the samples and experimental setup have been described, and that the

theory has been presented, it is time to move on to the experimental results.

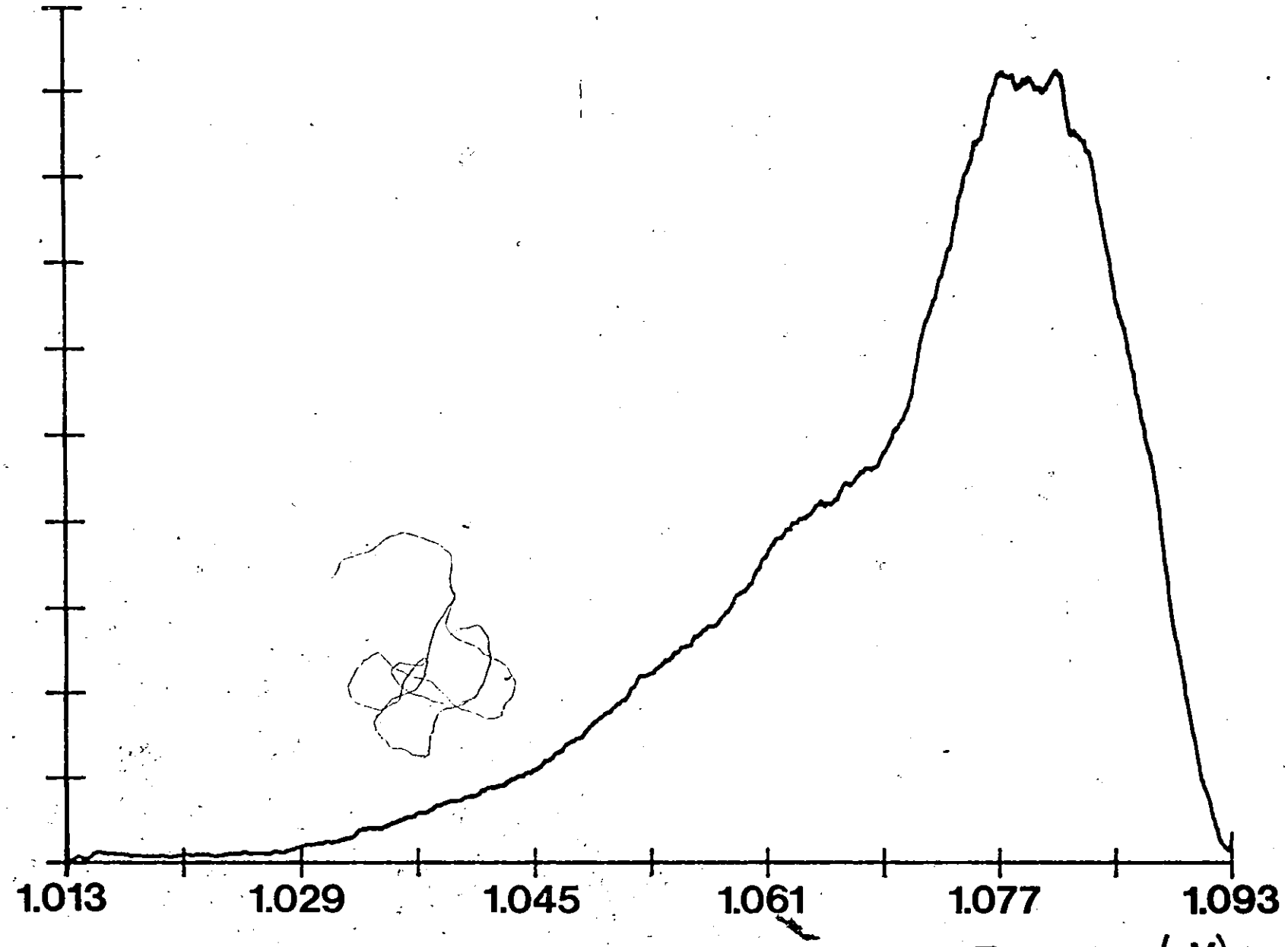

FIGURE IV.8 Infrared intensity vs photon energy

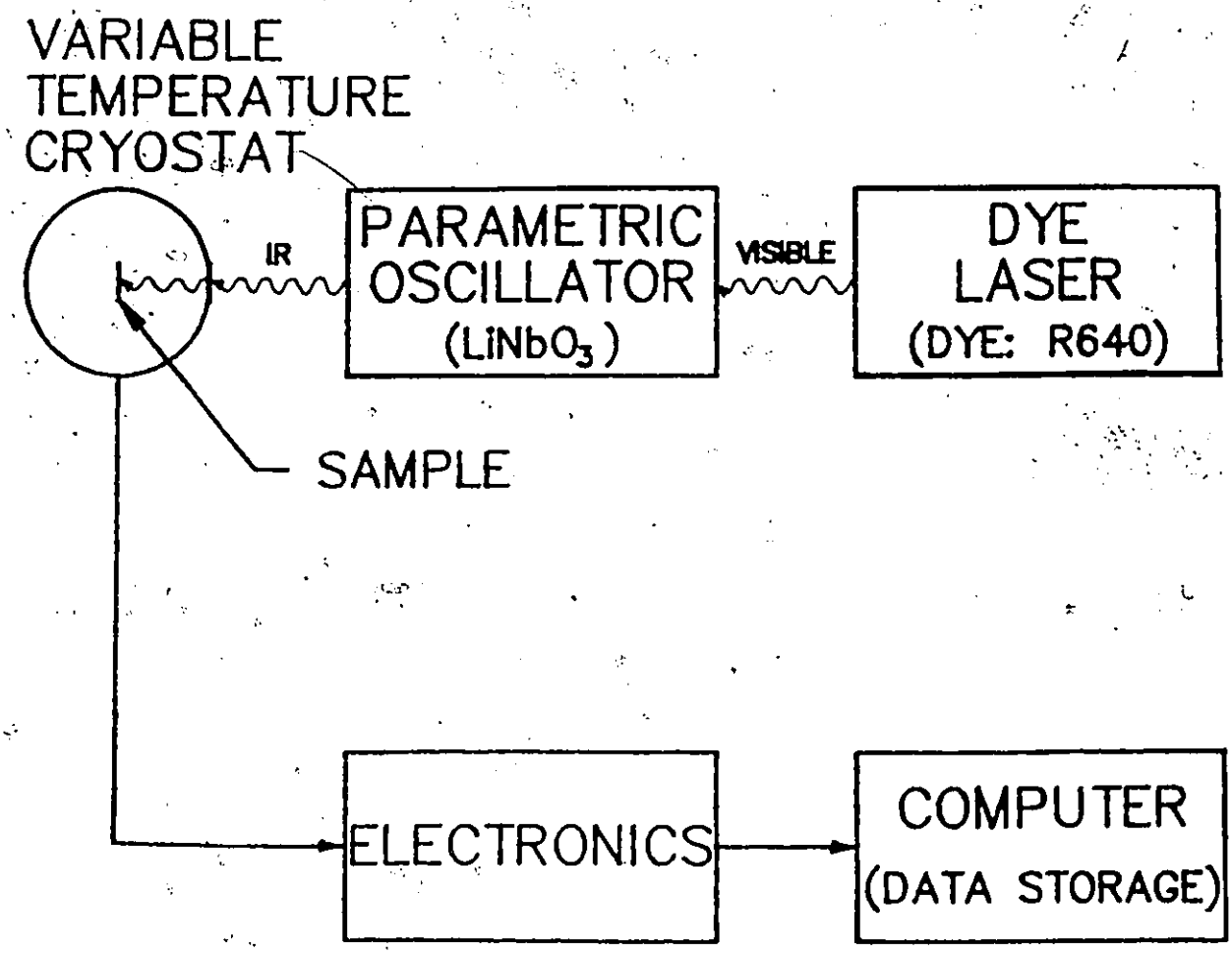

FIGURE IV.9 Experimental setup for high intensity infrared measurements

CHAPTER V EXPERIMENTAL RESULTS

V.1 INTRODUCTION

The experimental results will be presented and discussed in this chapter. The results from the transmission experiments will be followed by those from the one-photon photovoltaic effect. The chapter will conclude with the results from the two-photon photovoltaic effect.

V.2 TRANSMISSION EXPERIMENTS

The general transmission characteristics of the Cu_2O samples were much like any other semiconductor: high absorption for energies greater than the bandgap energy and much smaller absorption for energies less than this. In Cu_2O, the transitions are forbidden between band states at k=0, where the minimum bandgap occurs. The transmission step at 6050 Å in Figure V.1 is the red edge of Cu_2O; it occured at lower energy (or longer wavelength) than the energy gap. The sample thickness of roughly 500 μm produced so great a light attenuation that it was only at wavelengths where the sample became almost completely transparent that any significant amount of light could be detected, especially on a linear scale.

Other samples showed structure on this scale (Figure V.2) that was attributed to the oxidation or annealing technique used to produce the sample[39]. When the oxidation or annealing took place in an effective oxygen pressure close to the copper region in the phase diagram (Figure III.2), defects on an atomic scale, giving rise to an excess of copper beyond stoichiometric proportions in the crystal would be created. These defects would

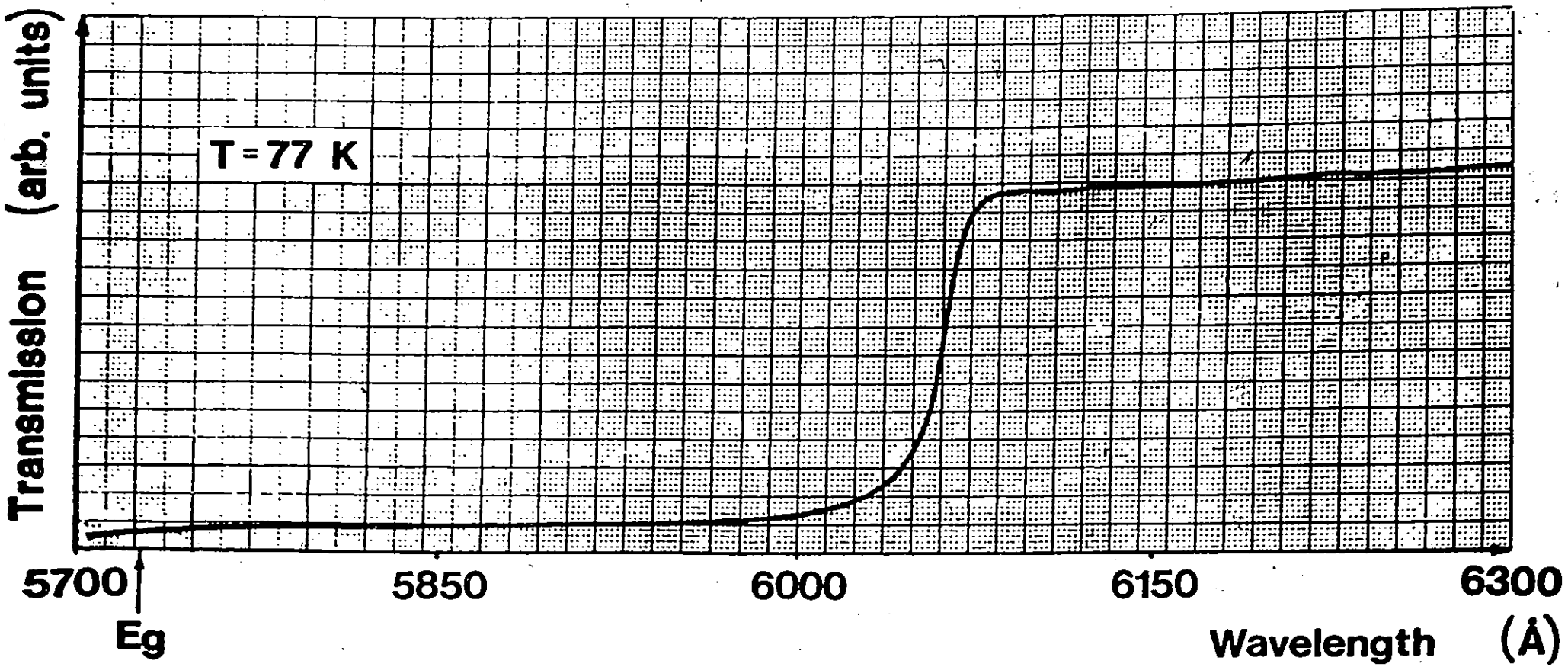

FIGURE V.1 General transmission characteristics of Cu_2O

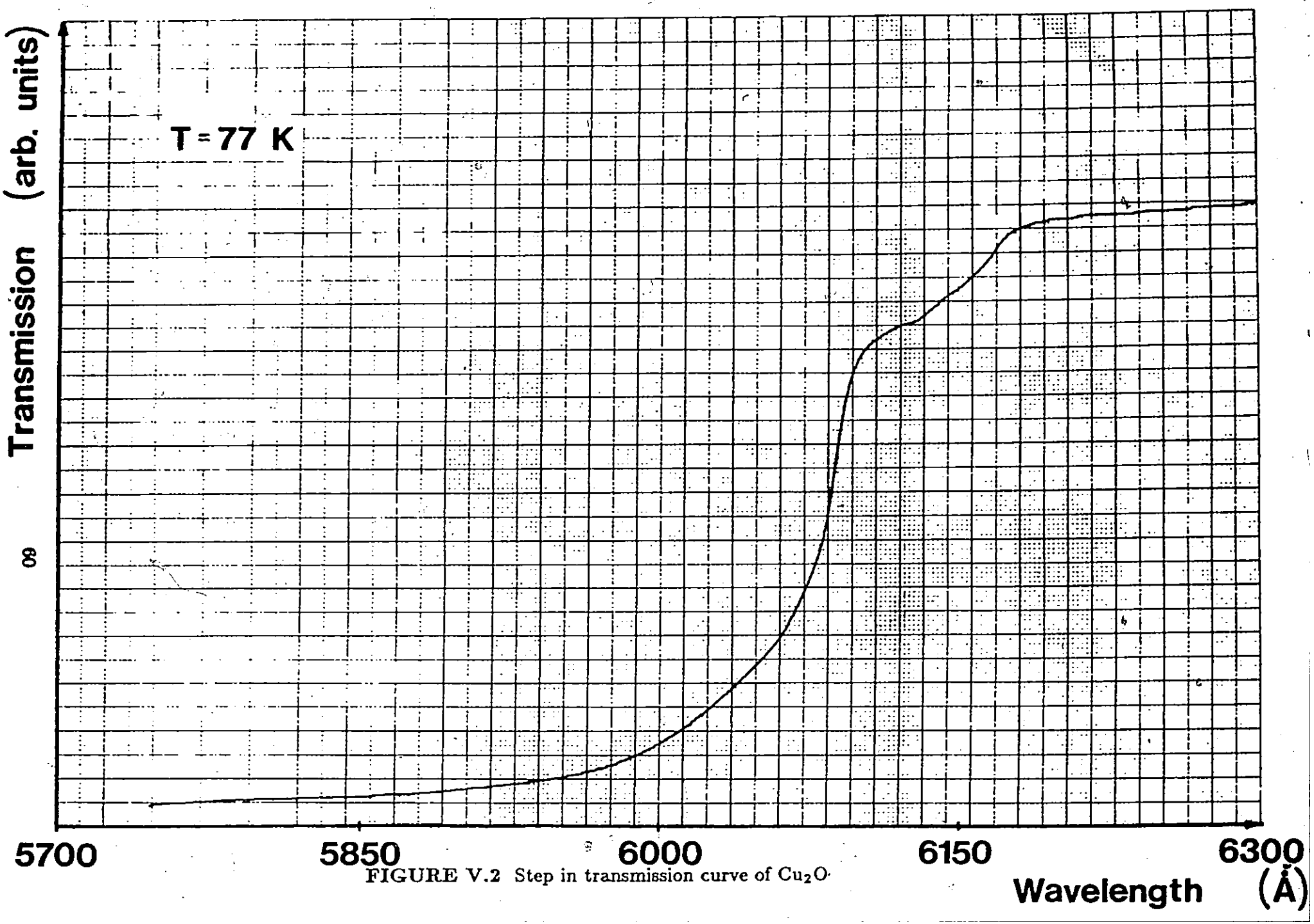

FIGURE V.2 Step in transmission curve of Cu_2O.

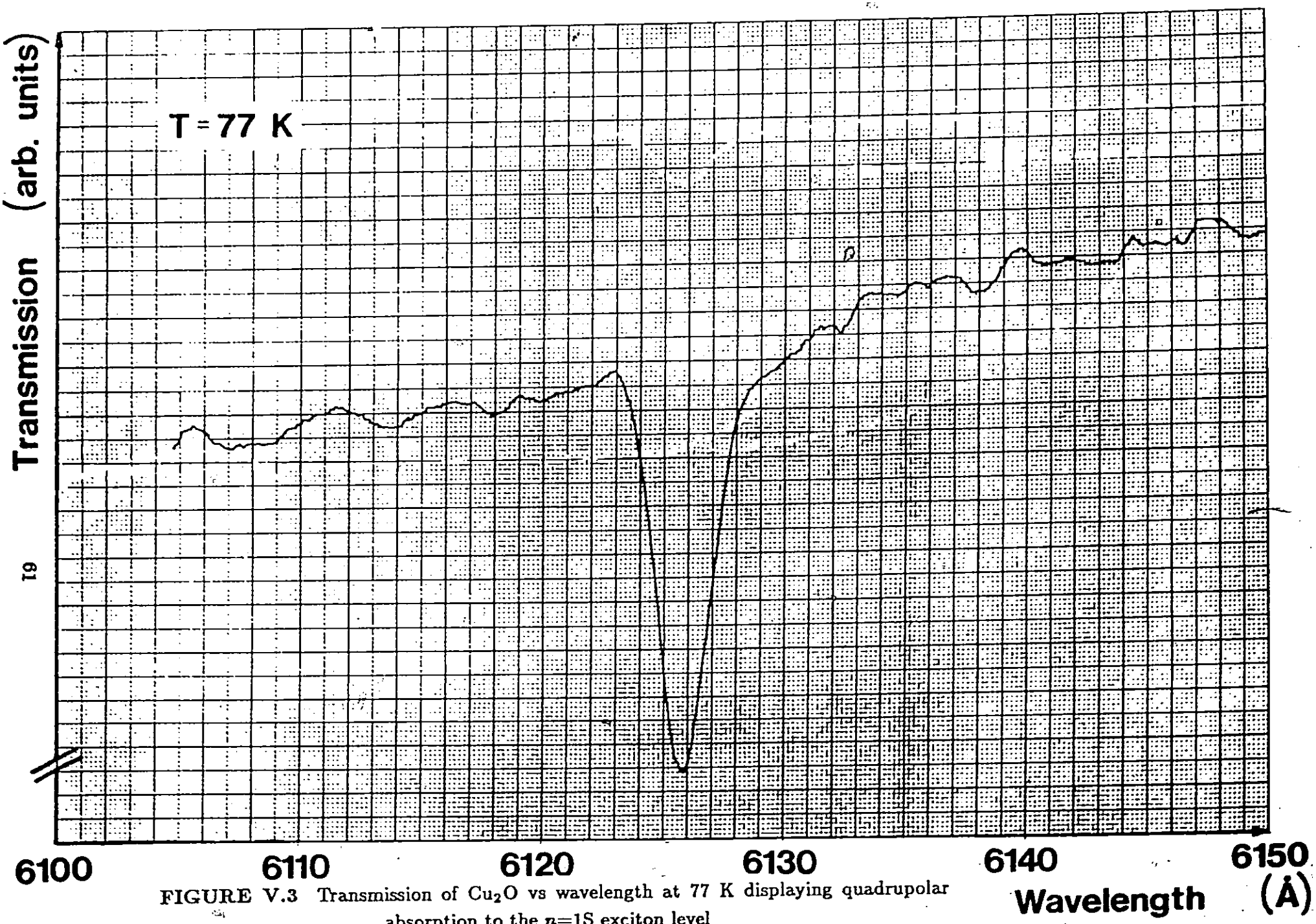

FIGURE V.3 Transmission of Cu_2O vs wavelength at 77 K displaying quadrupolar absorption to the n=1S exciton level

not cause major changes in the absorption constant except for the small plateau observed as in Figure V.2.

A dip on the long wavelength side of the bandgap appeared when the spectrometer slits were set at 100 μm, or under (Figure V.3). Further inspection found it to be one-photon electric quadrupolar absorption to the 1S exciton level. Its measured width at half-maximum absorption was 1.2 Å, indicating that the samples were of good quality[14].

At energies just below the bandgap energy, structure due to absorption to the n=2P and n=3P exciton levels was observed (Figure V.4 and Figure V.5). The slight shift from where the dips were expected was attributed to the use of a cryostat with a cold finger. The positions of the n=1 and n=2 exciton lines were then measured as a function of temperature using the CF204 cryostat (Figure V.6a and V.6b) and a second order least-squares fit performed on these values (solid lines). The results were found to agree, within experimental error, with the accepted[8,12,22,23] values.

V.3 LOW-INTENSITY PHOTOVOLTAIC EFFECT

a) Visible:

The observation of the yellow exciton series proved to be much easier using the photovoltaic effect. The visible exciton lines would all produce a photovoltage that was of the same order of magnitude. Exciton lines up to n=4P could be seen (Figure V.7). Once again, the wavelength shift was attributed to the use of the cold finger cryostat. The energy shift of the exciton lines with temperature was measured with the help of the large cryostat and heater (Figure V.8 *a*, *b*, *c*, *d*). At room temperature, no exciton lines were visible. As the sample was cooled, they became distinguishable at about 170 K. Then,

as the sample continued to be cooled, they shifted toward higher energies. Ultimately, their visibility decreased to the point where even the n=2P line was barely distinguishable because of a lack of phonon energy to dissociate them. For samples thicker than the one used for these measurements (30 μm), it is possible that this effect would have lead to a dip in the signal at the exciton energy. This meant that some sort of optimum temperature for exciton visibility could be found. The range of temperatures between 125 K and 75 K was found to yield the best results. Note that the temperature on the graphs is denoted by T*. This is the temperature that was measured using both the thermocouple and the diode. It was estimated to be accurate to within ±5 degrees. The exciton lines were shifted by about 10 Å from their accepted positions. This shift corresponded to a temperature difference of about 20 degrees, with the sample being warmer than expected. Speculation is that the sample would be at a higher temperature because both its sides were in good thermal contact with the heater. The thermocouple, forming only a point contact with the heater, and the diode, protected by its plastic casing, may not have been in sufficiently good thermal contact with it. Despite their somewhat qualitative nature, this series of measurements clearly demonstrated the changes that took place as the temperature was lowered.

Because of the high absorption coefficient in the exciton region, the Cu_2O thickness was kept relatively thin (< 50 μm) for one-photon measurements. The only drawback to thick samples for these measurements was that the photoresponse would decrease in magnitude because the diffusion length of the carriers created near the surface was not long enough to reach the Cu_2O/Cu junction.

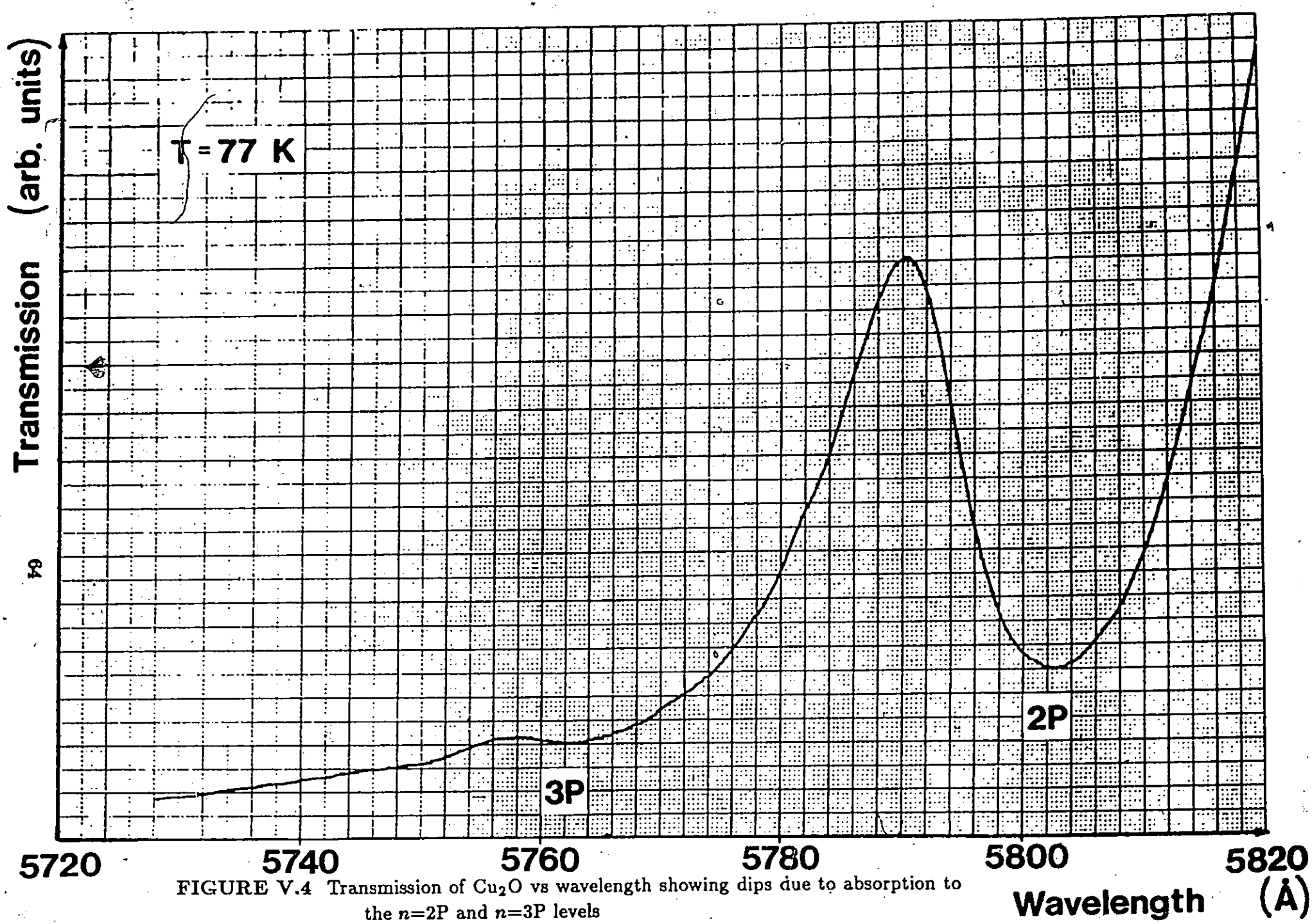

FIGURE V.4 Transmission of Cu_2O vs wavelength showing dips due to absorption to the n=2P and n=3P levels

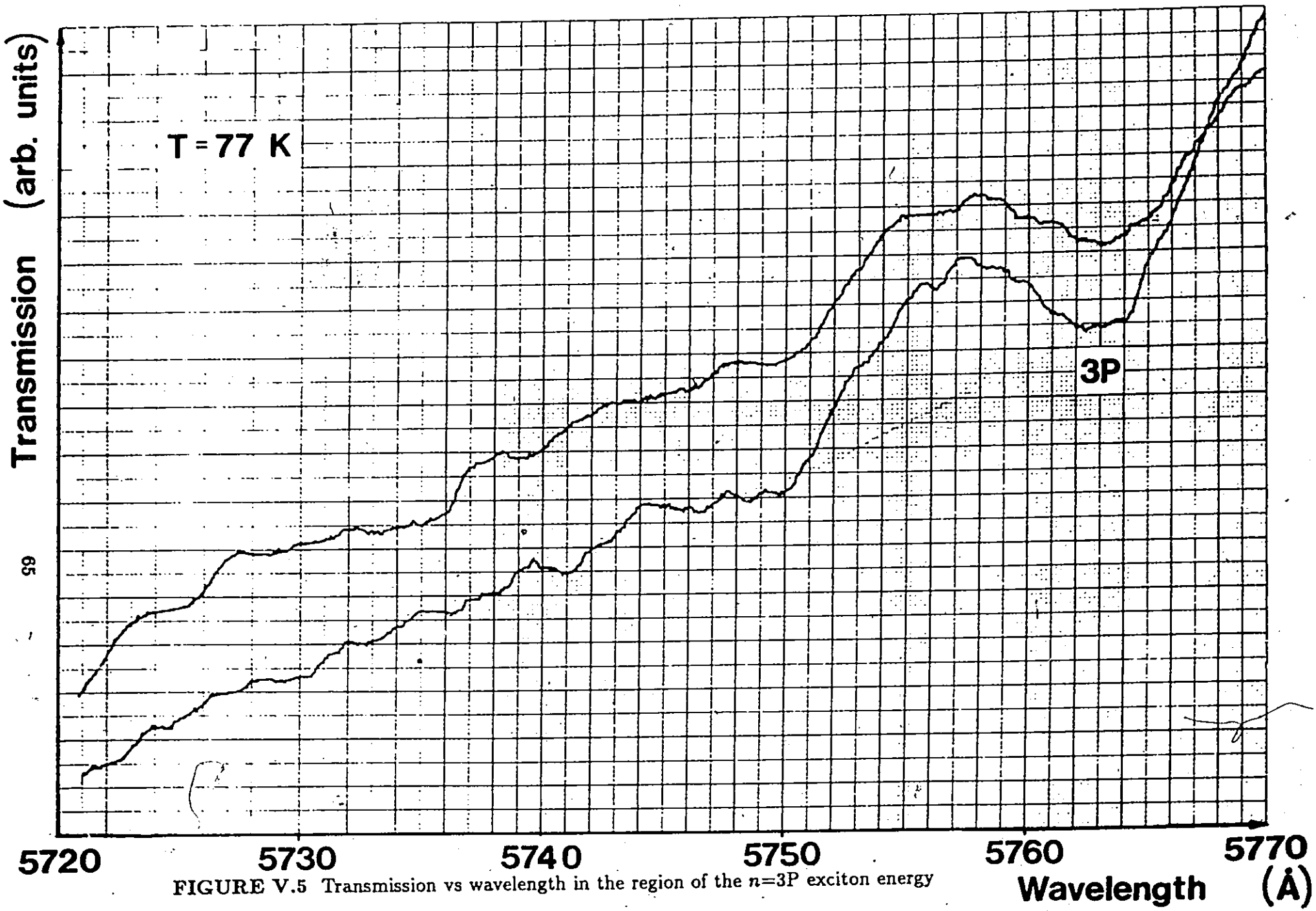

FIGURE V.5 Transmission vs wavelength in the region of the n=3P exciton energy

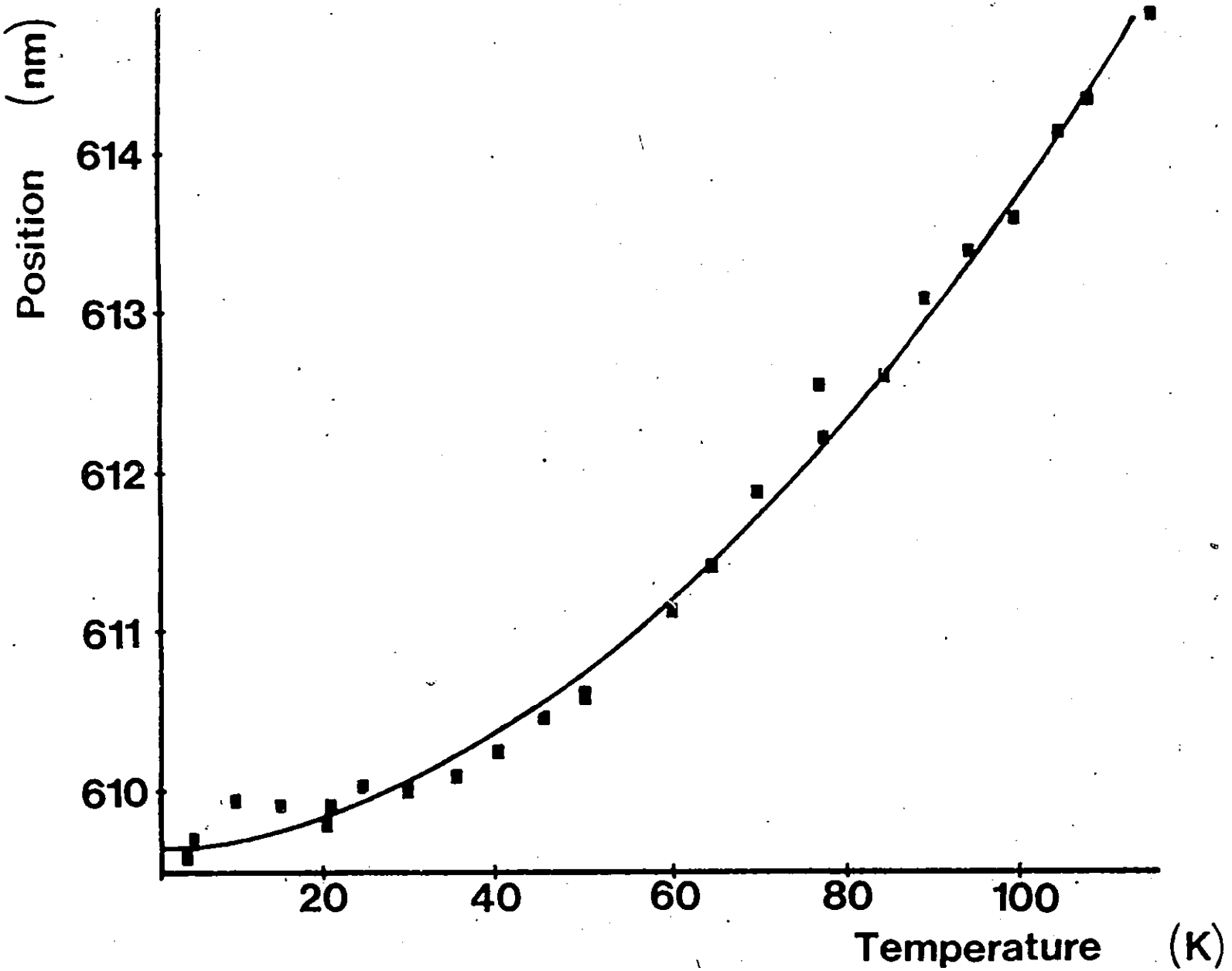

FIGURE V.6a) Position of the n=1S exciton line vs temperature

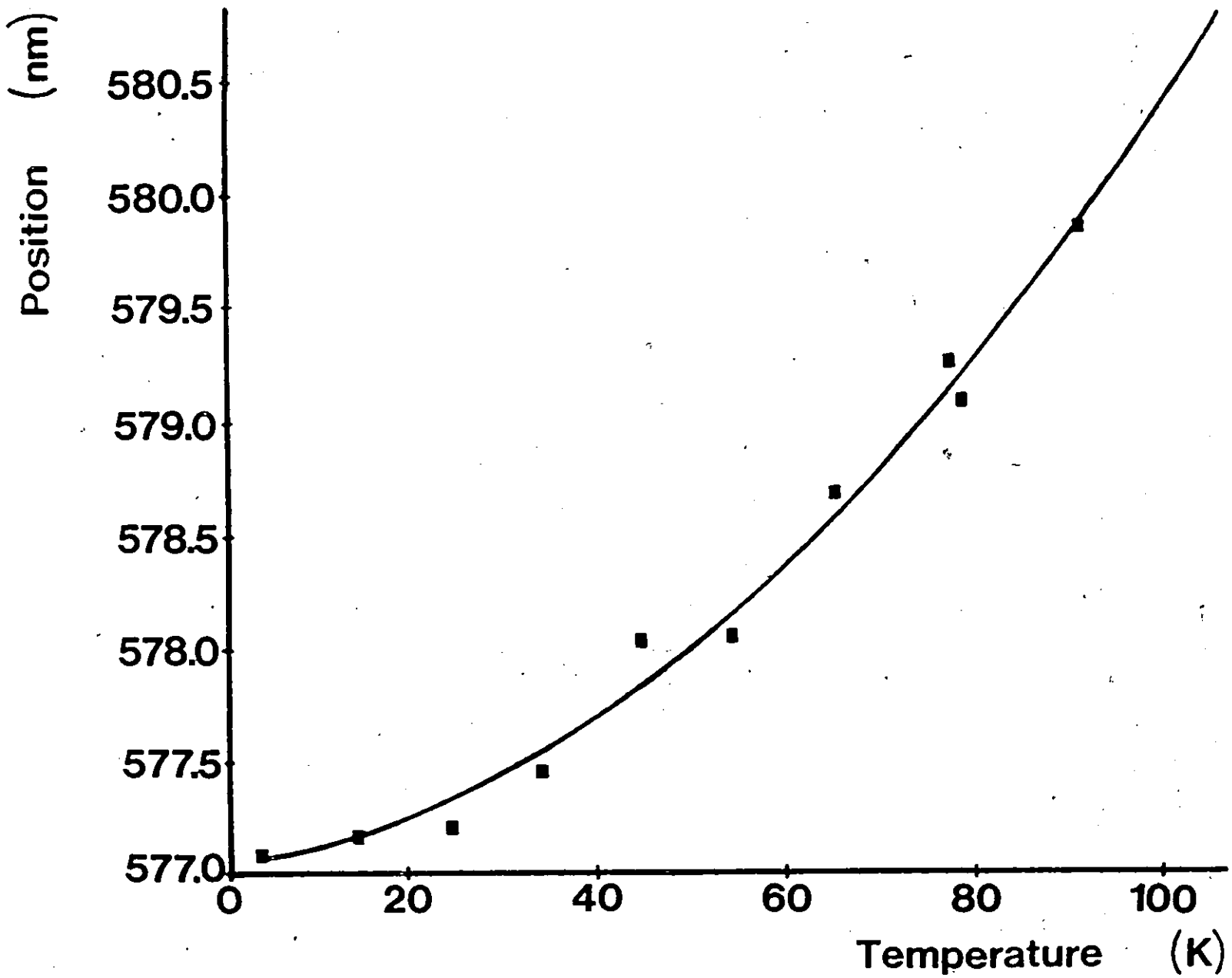

FIGURE V.6b) Position of the n=2P exciton line vs temperature

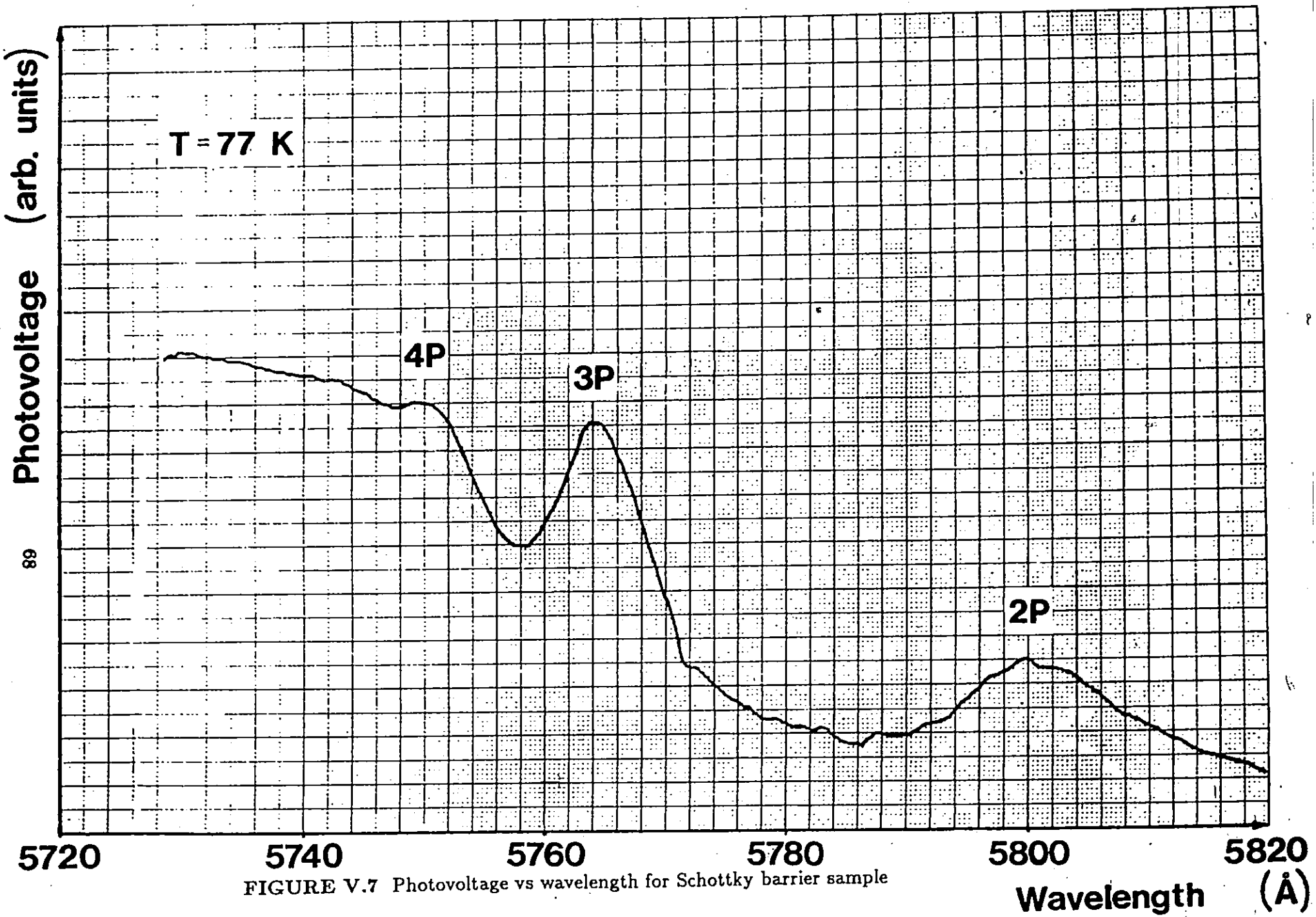

FIGURE V.7 Photovoltage vs wavelength for Schottky barrier sample

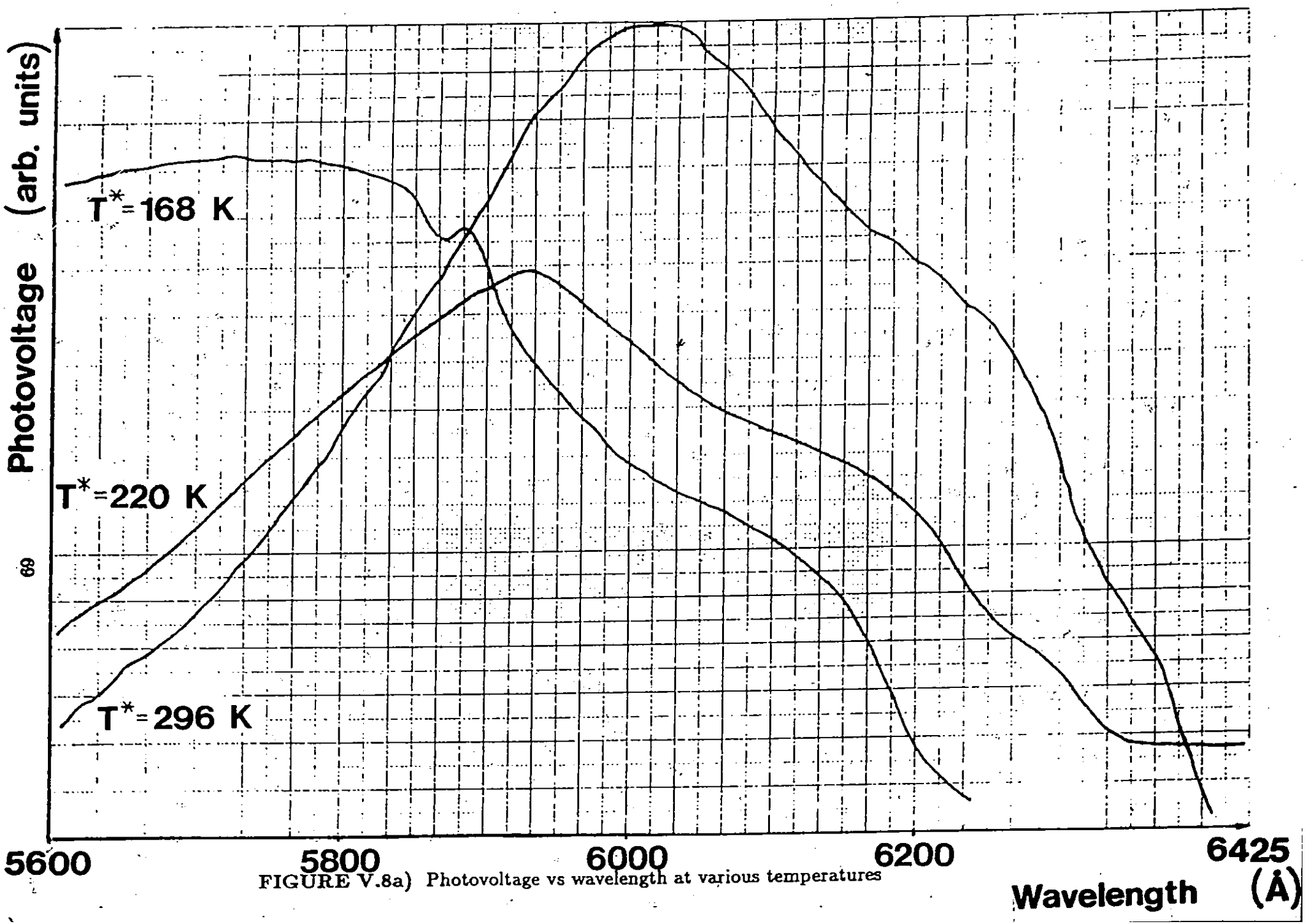

FIGURE V.8a) Photovoltage vs wavelength at various temperatures

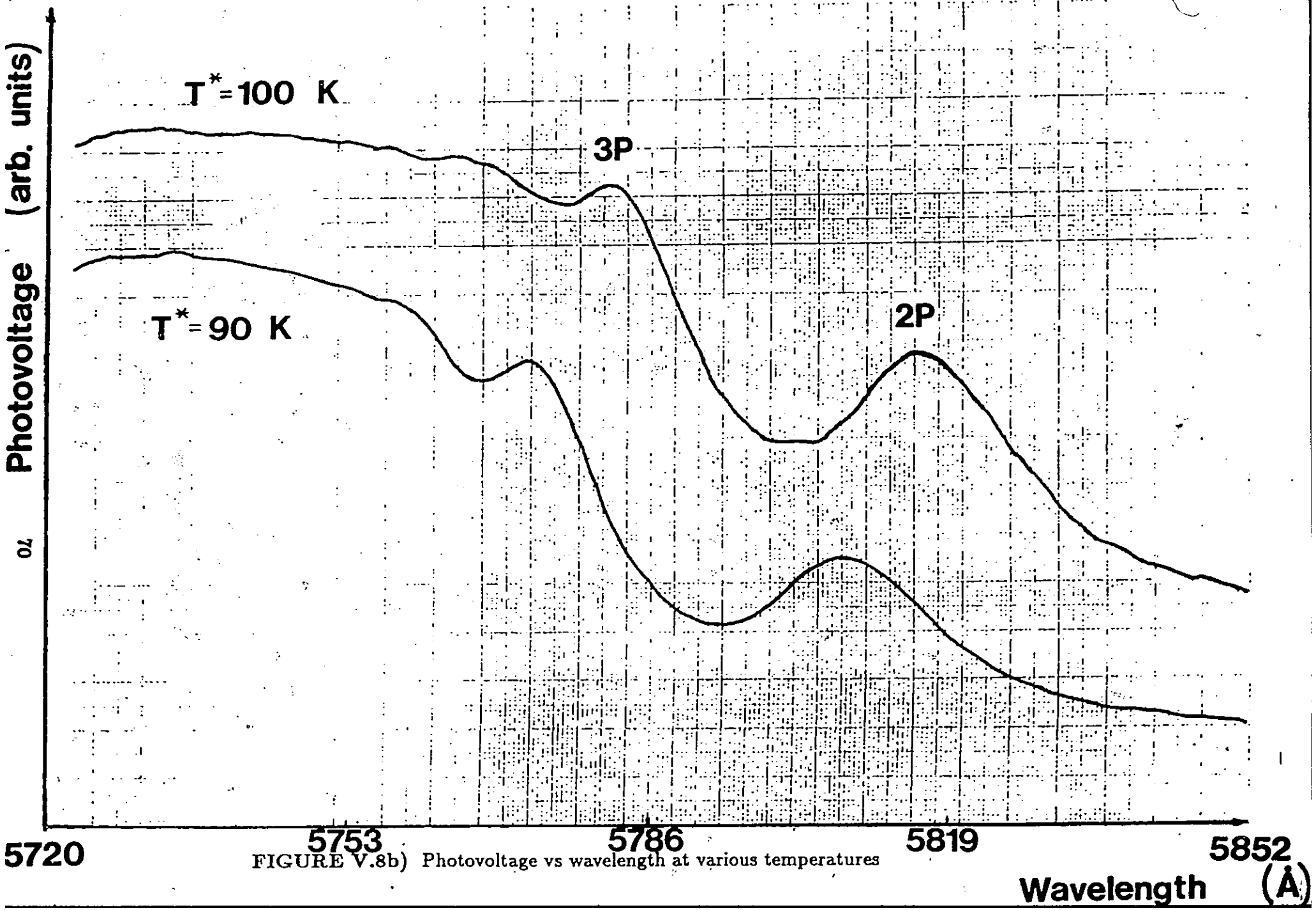

FIGURE V.8b) Photovoltage vs wavelength at various temperatures

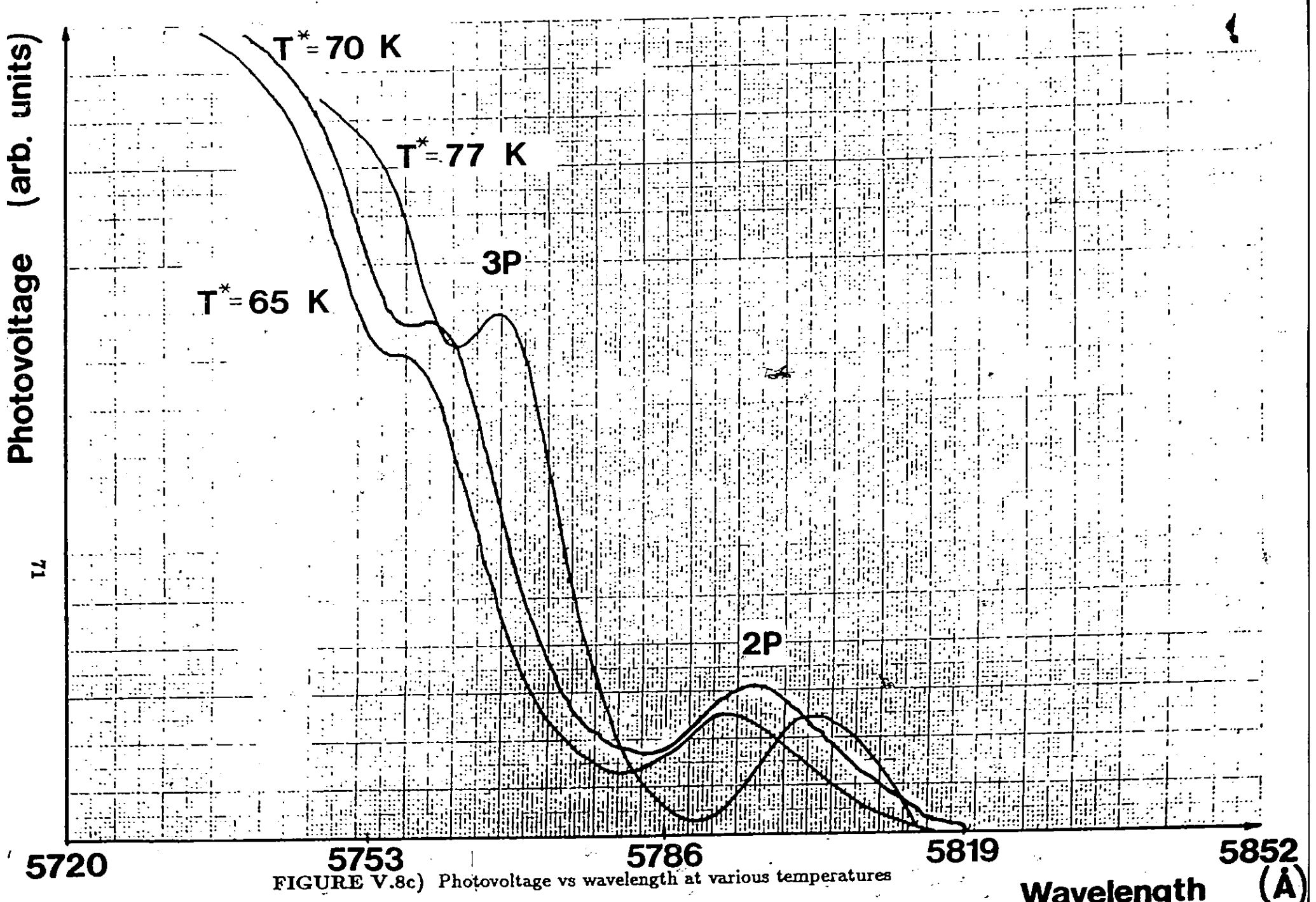

FIGURE V.8c) Photovoltage vs wavelength at various temperatures

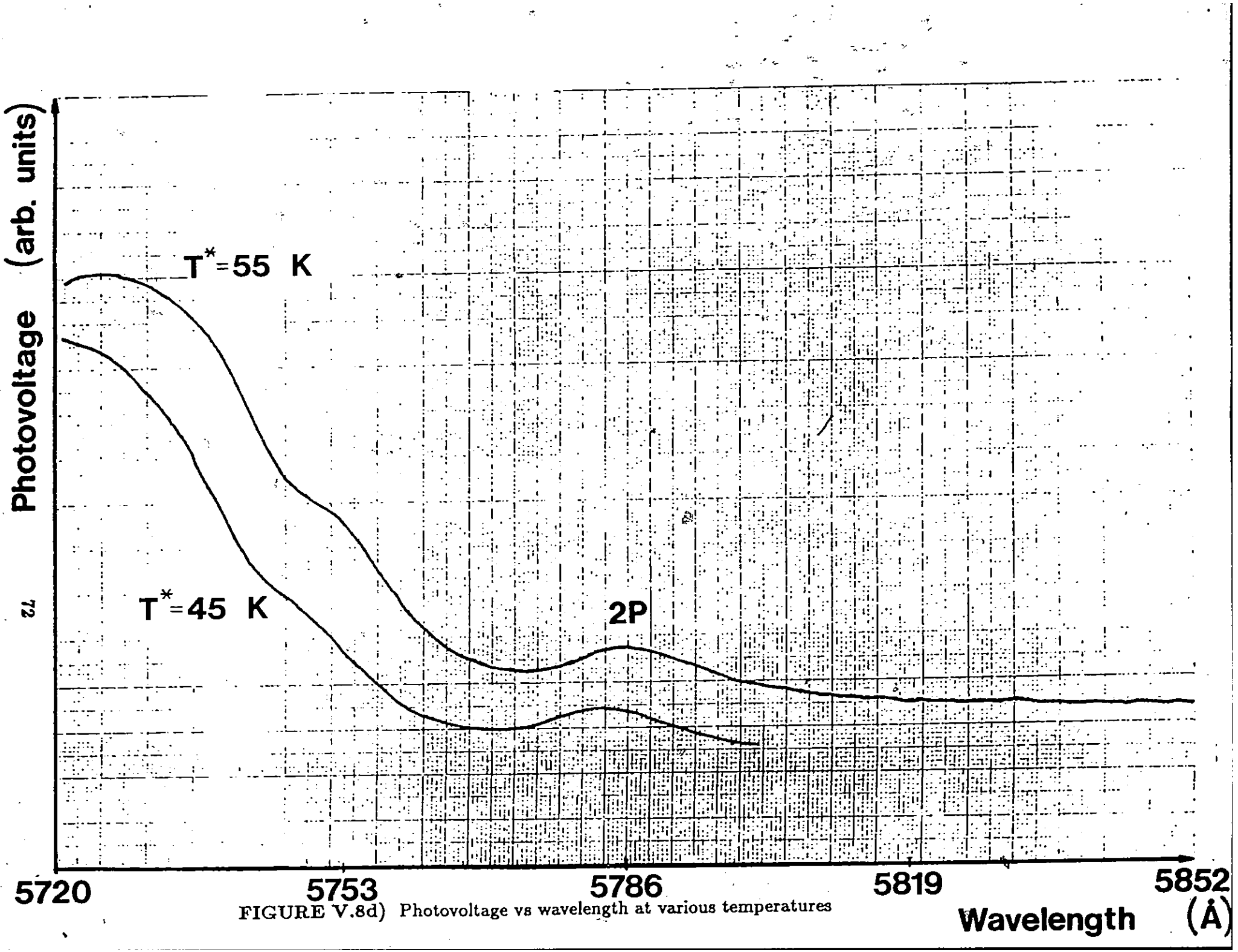

FIGURE V.8d) Photovoltage vs wavelength at various temperatures

b) Infrared:

As mentioned before, the contribution due to the two-photon effect was expected to be very small. To help detect it, an effort was made to eliminate any other signals produced in the sample at the infrared wavelengths close to 1.15 μm.

Preliminary scans with the spectrometer showed that there was indeed a one-photon signal produced in the samples. In part, this was found to be due to the photoemission of holes, denoted by I_0 in Figure II.4*a* into Cu_2O, in which the threshold photon energy corresponds to the barrier height associated with the Cu_2O/Cu contact[24]. This barrier height has been measured to be under 1.0 eV[2,24], and is not changed by the application of a bias voltage. Other metals could have been evaporated onto a Cu_2O substrate to produce a sample with a higher energy barrier. Since most metals other than copper reduce Cu_2O to form essentially a Cu_2O/Cu junction, the barrier height would still have been in the 0.7 to 1.0 eV range. This contribution, of the same polarity as the two-photon absorption signal, could therefore not be eliminated from the total signal. This was of little importance for scans performed in the visible because the signal from conduction band electrons in Cu_2O dominated as expected[2]. It could be a problem, however, when attempting to detect two-photon absorption.

The second contribution, denoted by I_0 in Figure II.4*c*, consisted of the photoemission of electrons from the Cu into the Cu_2O[24]. Copper electrons would be thermally excited into higher lying states, diffuse across the potential barrier and into the Cu_2O conduction band states where they would eventually recombine. Transport by drift would not occur because the field opposed the direction of travel. This thermal electron injection was of

opposite polarity to the signal due to two-photon absorption. By applying a reverse bias to the sample, the potential barrier that the electrons had to overcome could be raised to the point where this component could be eliminated. Experimentally, the application of the reverse bias voltage was found to slightly improve the signal-to-noise ratio. Scans with and without bias voltage performed in the limited range near half the exciton and bandgap energy showed no structure.

V.4 TWO-PHOTON PHOTOVOLTAIC EFFECT

Finally, the time had come to perform measurements on the Cu_2O/Cu photovoltaic samples under high intensity. To do so, use was made of the CMX-4/IR parametric oscillator. A filter was inserted between the parametric oscillator and the sample to eliminate the light at the unwanted pump wavelength. Then, a converging lens of 5 cm focal length was inserted to achieve the highest possible local intensity on the sample

With the temperature of the $LiNbO_3$ crystal set at 370° C and pumping with Rhodamine 640 it was hoped that the whole of the yellow exciton series could be scanned. All of the energies required to observe the excitons in two-photon absorption, except for n=1S, were located near the peak IR power. For the n=1S exciton, the required wavelength was too far away from the peak intensity; the signal became lost in noise.

Thicker samples (80 μm) were used for these measurements since the two-photon absorption coefficient is much lower than for one-photon absorption. Initial measurements were performed without bias voltage (Figure V.9). No exciton structure was discovered in the photoresponse spectra. When compared with the reference intensity (presented again as Figure V.10 for convenience), it was quite obvious that the one-photon contribution had

not been eliminated.

The next step consisted of the application of a reverse bias to raise the potential barrier that the photoexcited copper electrons had to cross, thus eliminating this component of the signal. Reverse bias occured with the semiconductor negative and the metal positive. Exciton dissociation and the widening of the depletion width were additional positive effects of the bias voltage.

With an applied reverse bias of 1 Volt, a change occured near the peak signal. Although the general shape due to one-photon absorption remained, a second peak became visible in the spectra (Figure V.11). This new signal was found to become more prominent as the bias voltage was increased (Figure V.12). A maximum of 20 Volts was applied to the sample. Under this bias voltage, the new signal, located at C in Figure V.13*a*, was found to be the most prominent. On this diagram, the general shape of the curve was mainly due to the variation of the incident intensity. In particular, the structure at A was due to a similar variation in the incident intensity. The peak and subsequent decrease in the signal at B was also due to the variation of the intensity.

Unfortunately, this scan was not performed at the same sample temperature as the others. Initially, it was planned to operate between 125 K and 75 K to obtain maximum exciton visibility. Once measurements began and the two-photon signal was observed, attempts to improve its visibility lead to a variation in sample temperature, leading to a temperature of 45 K for Figure V.13. For similar reasons, the reverse bias voltage was varied. The two-photon signal became more visible as the bias voltage was increased.

The signal at C was attributed to two-photon absorption in the layer of Cu_2O, pro-

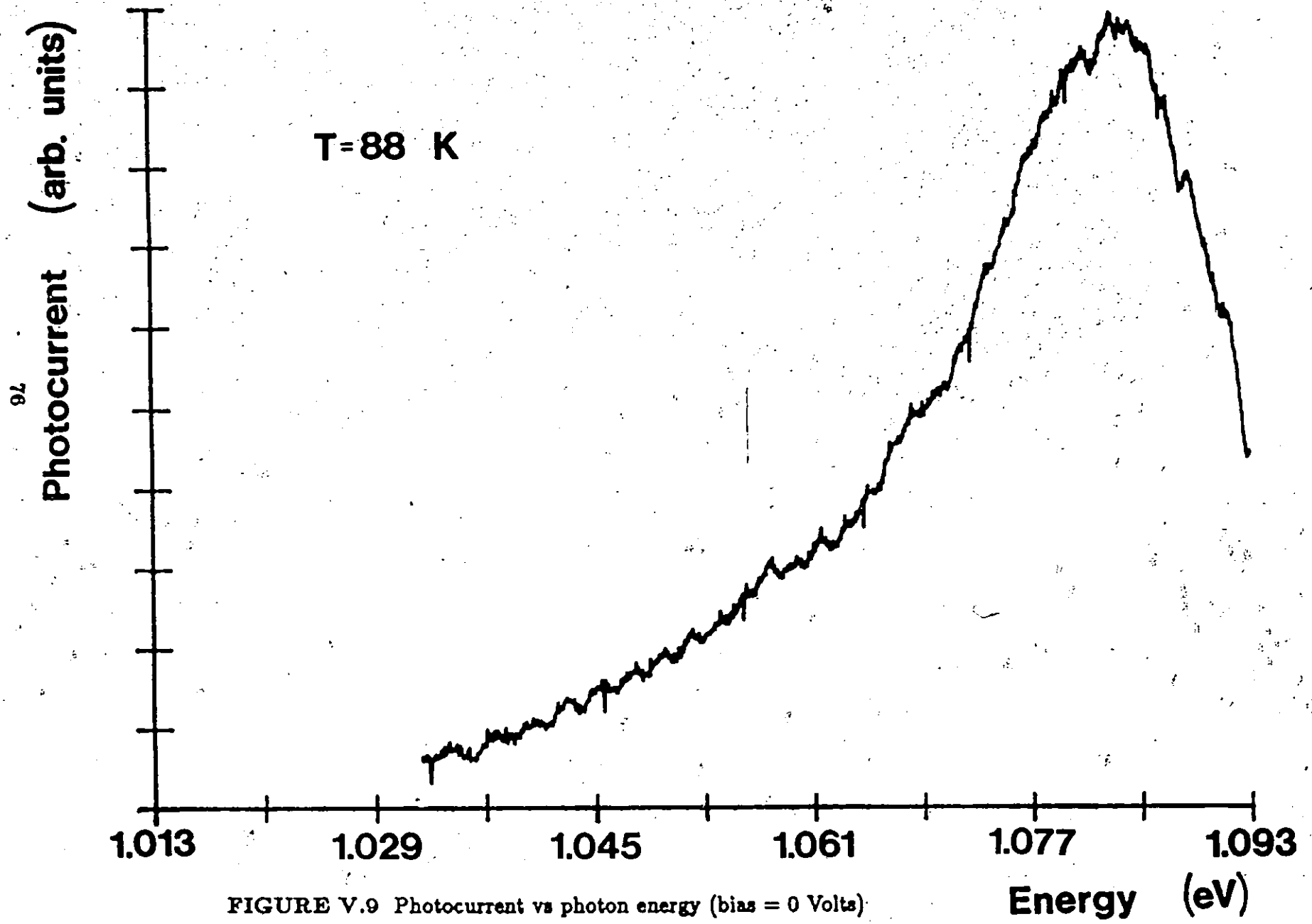

FIGURE V.9 Photocurrent vs photon energy (bias = 0 Volts)

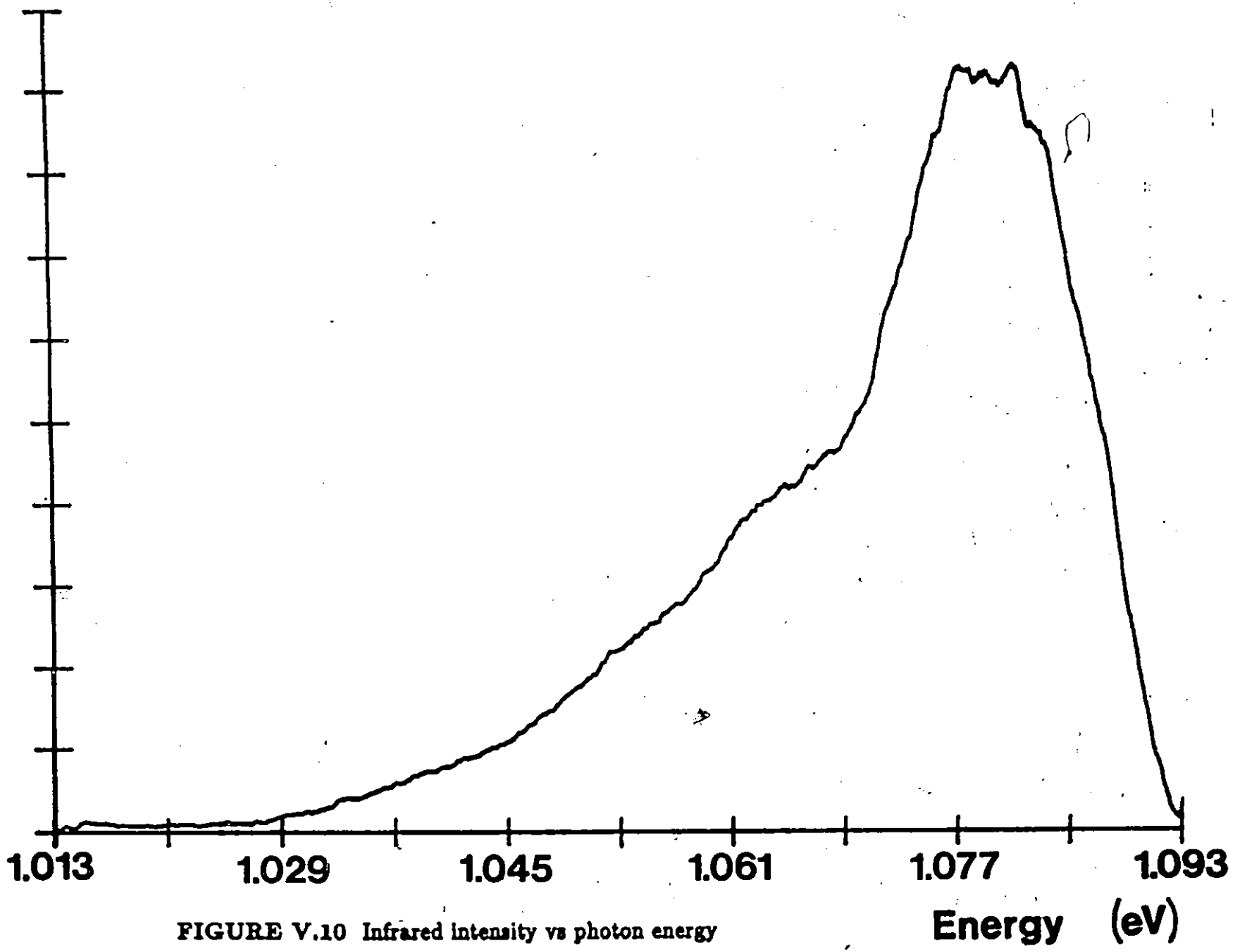

FIGURE V.10 Infrared intensity vs photon energy

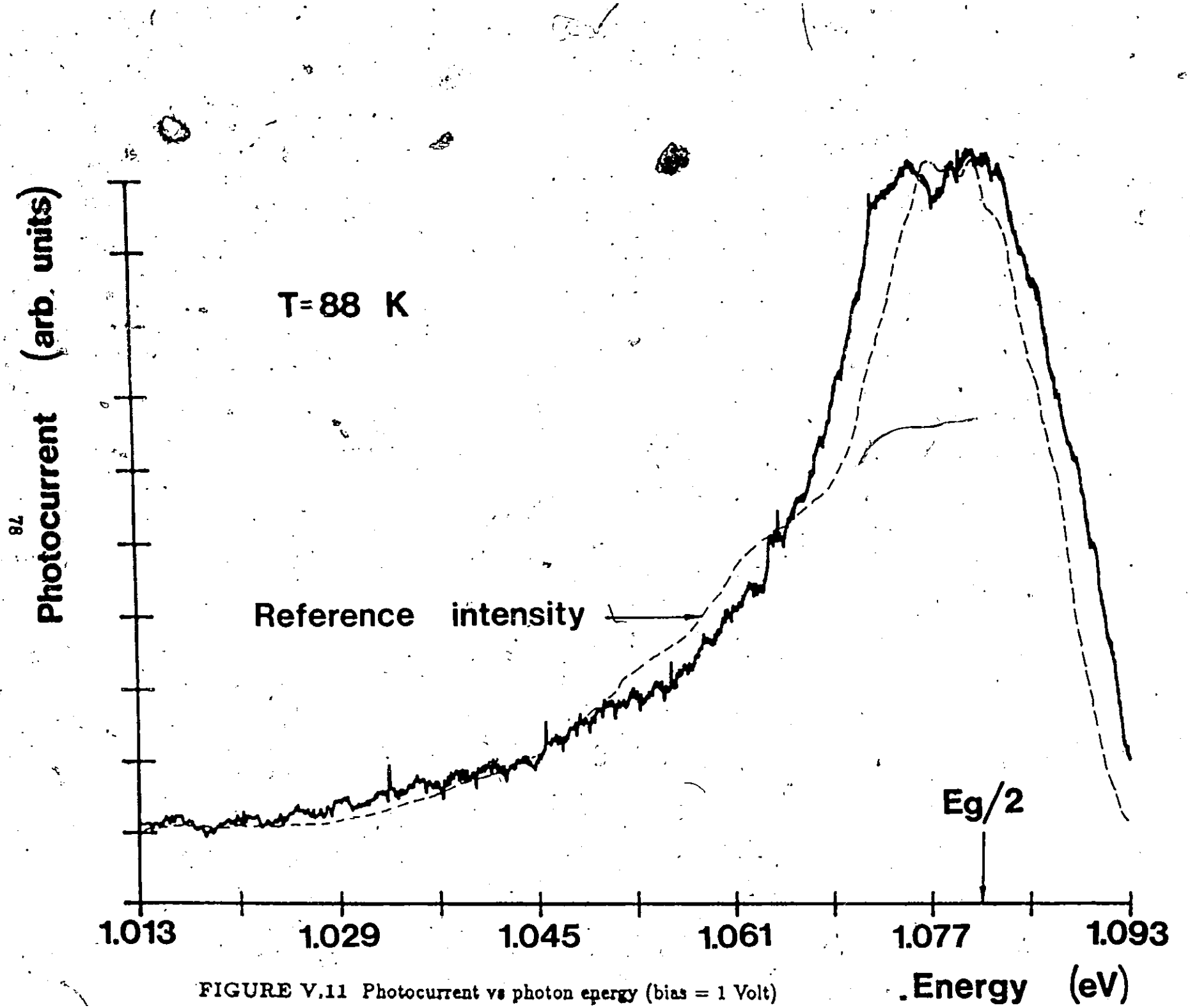

FIGURE V.11 Photocurrent vs photon energy (bias = 1 Volt)

ducing conduction band electrons that reached the Cu-Cu_2O junction and were injected into the copper. By assuming that the one-photon signal was proportional to the intensity and subtracting this contribution from Figure V.13*a* resulted in Figure V.13*b*, an attempt to isolate the two-photon photocurrent. Both band-to-band two-photon absorption and absorption to exciton levels followed by thermal or electric field exciton dissociation would contribute to the two-photon signal. This interpretation was supported by the fact that no such signal was observed under low-intensity infrared illumination when the bias voltage was applied.

The signal was expected to shift as the temperature of the sample was varied. This shift is not very large; using Figure II.3 as a guideline, the position of the two-photon signal was expected to shift by about 15 meV between 150 K and 4.2 K. Efforts to detect this shift were inconclusive. This was partially due to a slight energy shift (reaching up to 5 meV) occuring in the reference intensity from run to run. This shift may have been the result of variations of about 0.2° C in the temperature of the $LiNbO_3$ crystal.

Attempts were then made to resolve the individual exciton lines. Slow scans were performed over the narrow region where the exciton lines were expected to be (Figure V.14). The signal failed to display any clear sign of exciton lines. The structure seen on the graph was almost certainly random noise. Since the energy difference between the exciton lines varies very little as the temperature changes, the matching of the energy differences between the exciton lines and the structure observed in Figure V.14 was attempted. Even if slight positional shifts of the exciton lines occured because of temperature or electric field effects, their presence should have been detected using this method. It wasn't. Failure

to resolve the exciton lines was attributed to a combination of linewidth, pulse-to-pulse noise and relatively low intensity (3 kW/cm^2 vs 100 MW/cm^2 peak intensity[14] produced by fixed wavelength lasers in experiments employing two light sources) of the parametric oscillator.

To model the signal due to two-photon absorption, the observed signal was assumed to be mainly due to band-to-band two-photon absorption. If the one-photon curves are considered, the exciton lines are seen as structure on the general shape of the curves; see for example the curves recorded at 77 K, 70 K and 65 K (Figure V.8c). The small experimental variation of the magnitude of the two-photon signal with temperature is also an indication that band-to-band absorption is responsible. If it were due to excitons, the signal would be expected to disappear at low temperatures. Furthermore, it was assumed that the two-photon photocurrent was basically due to conduction band electrons generated in the depletion layer. When no bias is applied to the sample, no signal due to two-photon absorption is observed. As the bias voltage is increased and the two-photon absorption becomes visible, the depletion layer becomes thicker and the depletion current increases. The diffusion current shouldn't vary because two-photon absorption takes place in the volume of the sample, and is not limited to a surface layer.

The two-photon photocurrent predicted by equations (9) and (27) was then calculated by computer. The incident flux was obtained from the measured values of intensity versus photon energy saved on diskette via the pyroelectric detector and analog-to-digital converter. Point by point, energies were put into the two equations and the resulting curves plotted (Figure V.15) in the same energy range as Figures V.9 to V.12. No attempt was

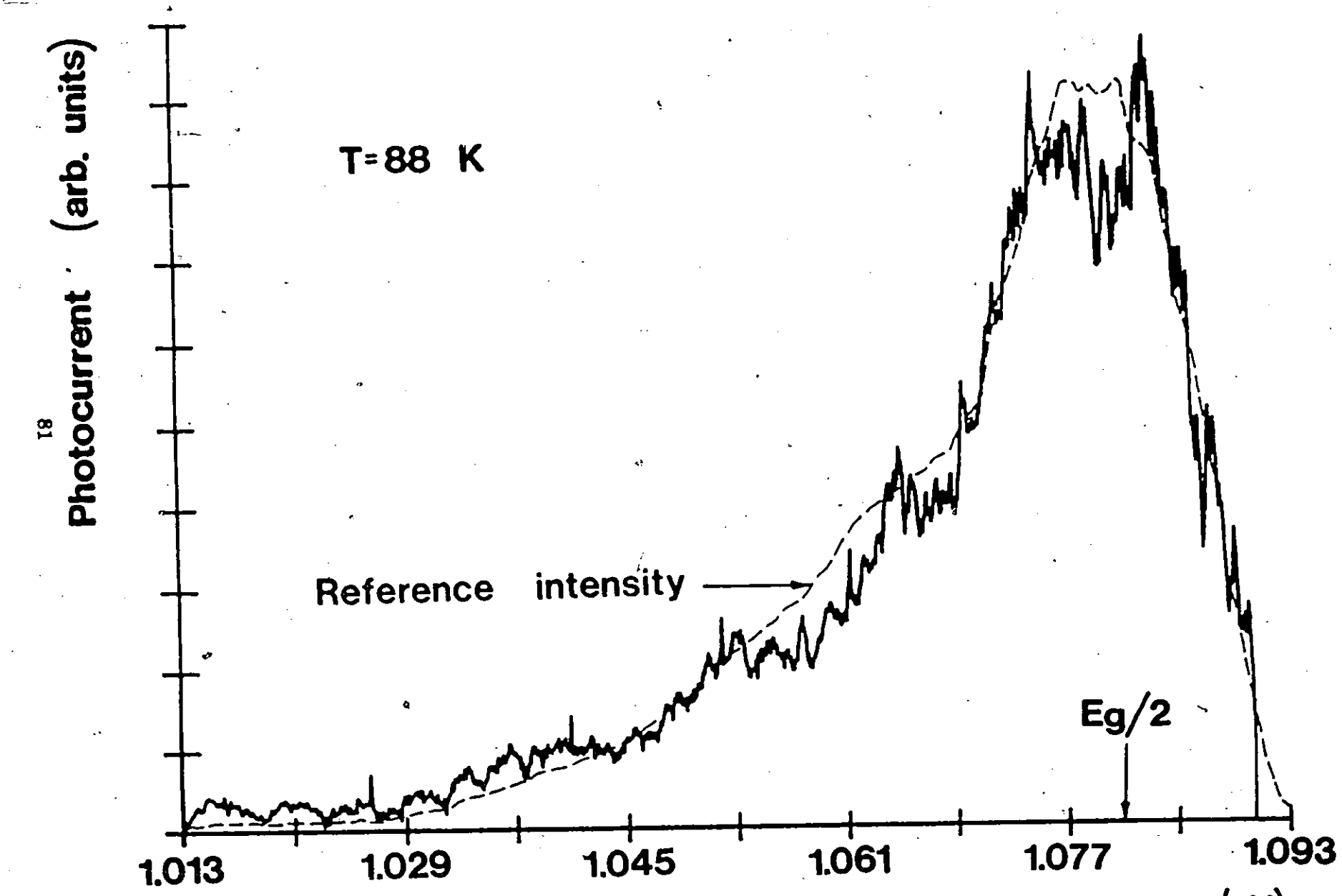

FIGURE V.12 Photocurrent vs photon energy (bias = 6 Volts)

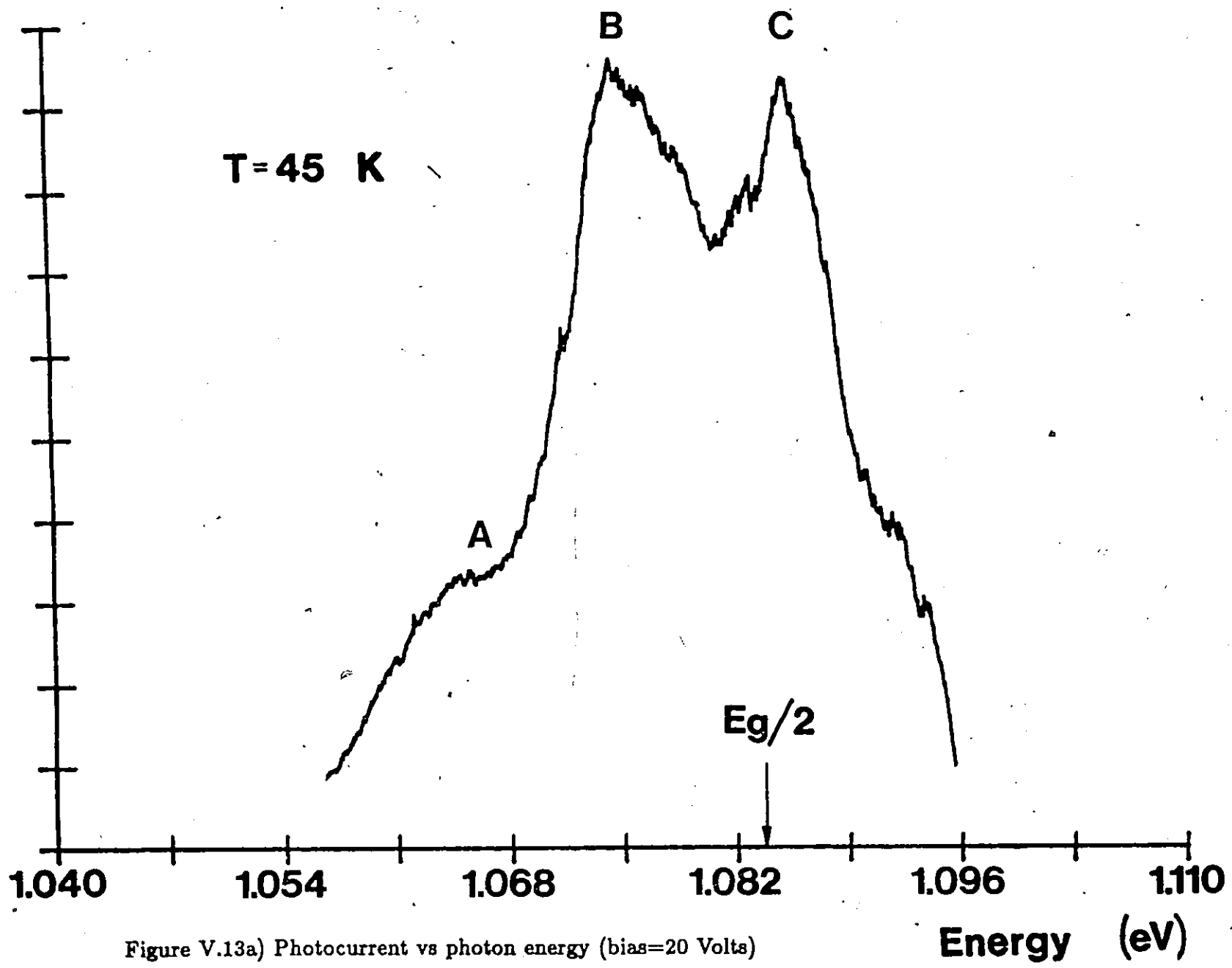

Figure V.13a) Photocurrent vs photon energy (bias=20 Volts)

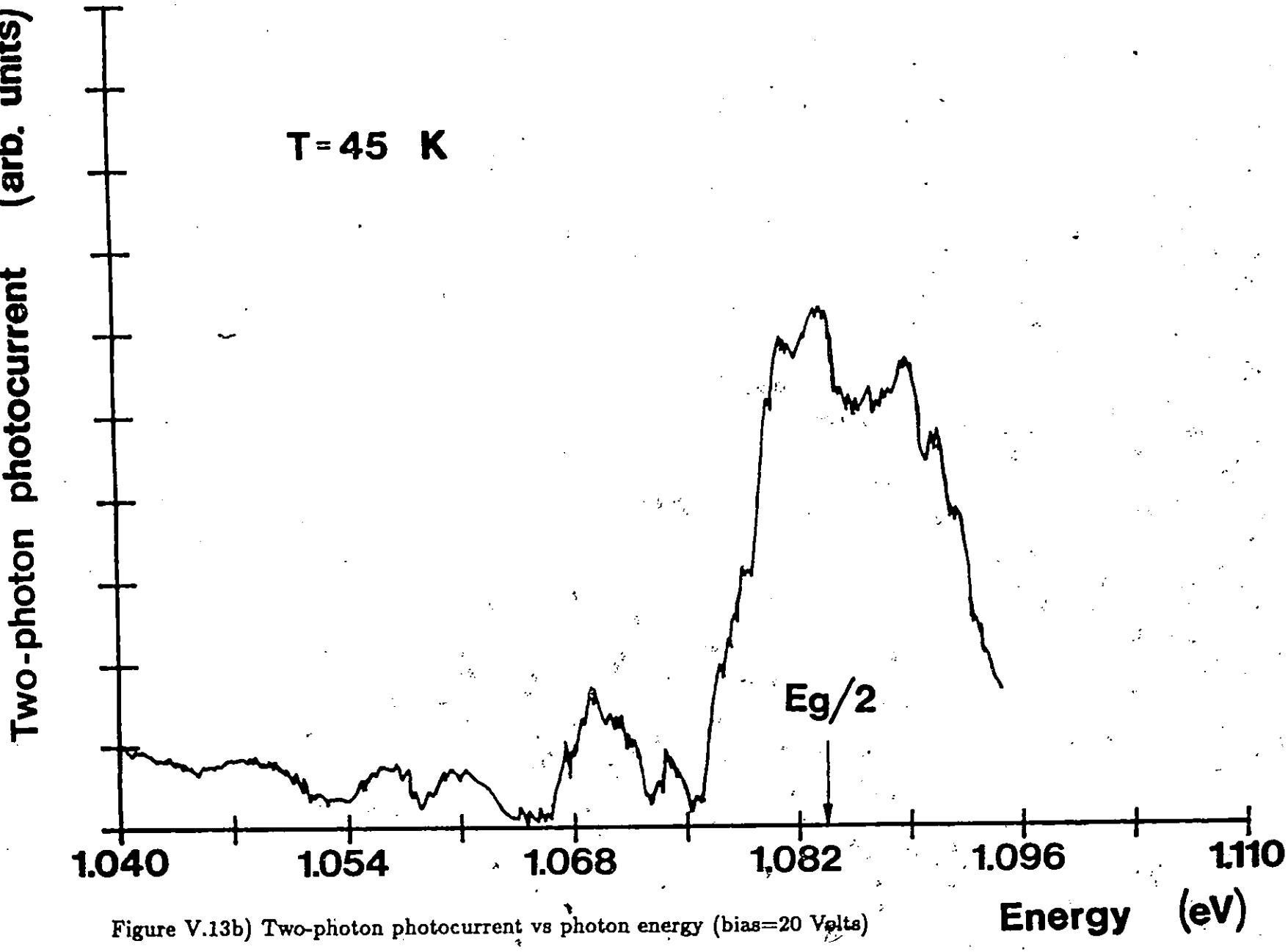

Figure V.13b) Two-photon photocurrent vs photon energy (bias=20 Volts)

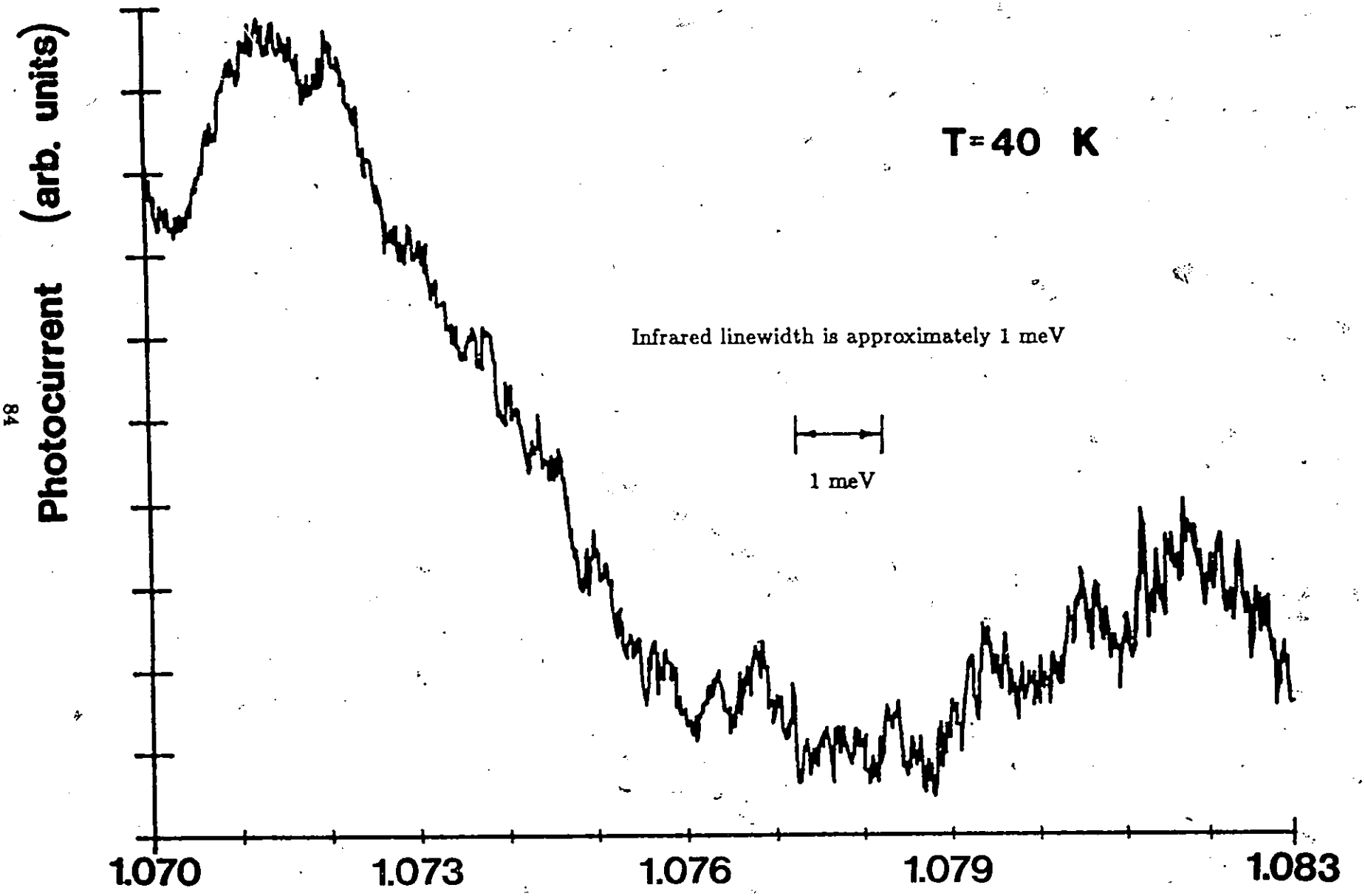

FIGURE V.14 Photocurrent in exciton region vs photon energy (bias = 20 Volts)

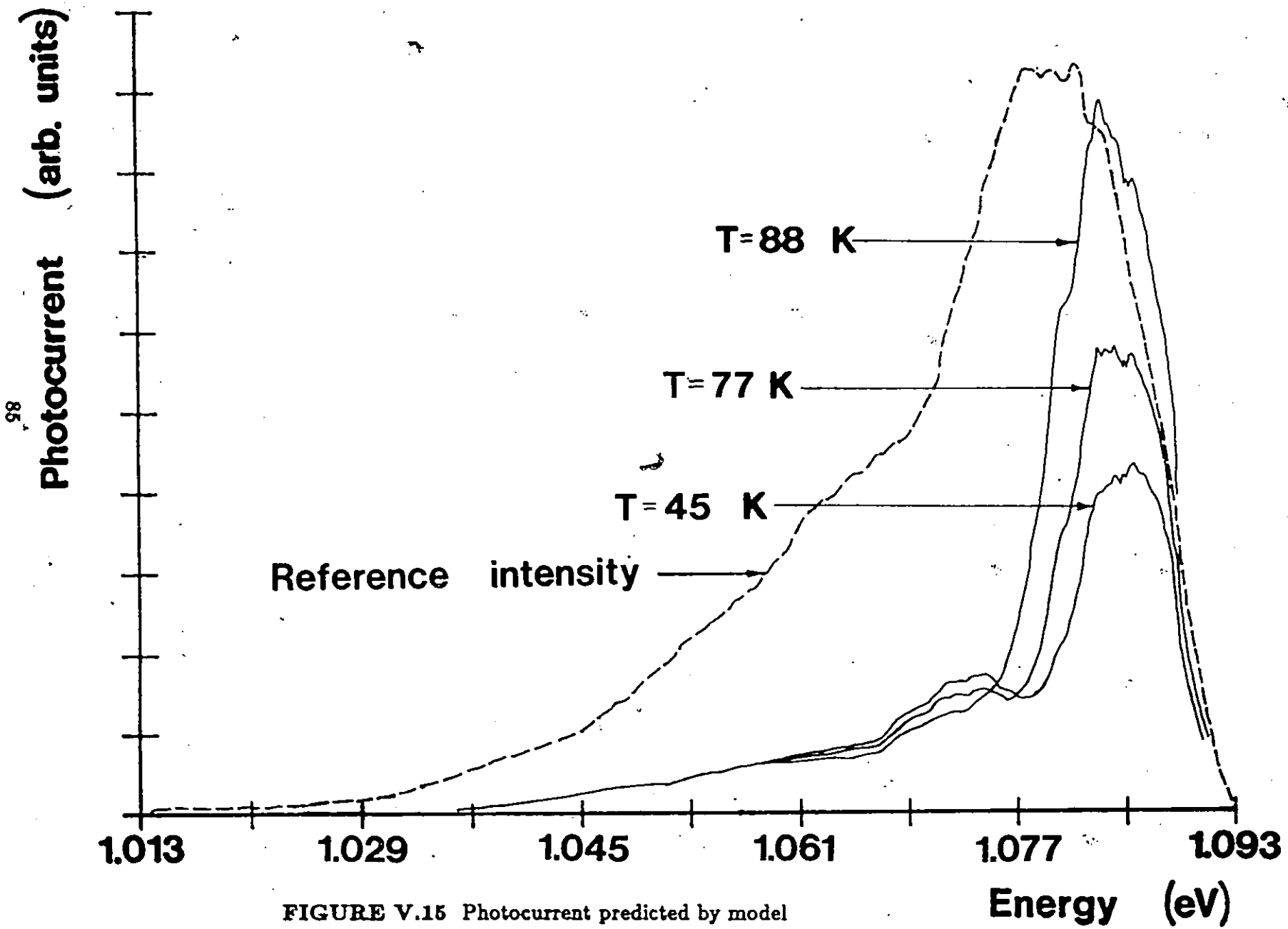

FIGURE V.15 Photocurrent predicted by model

made to predict absolute values of photocurrent. The curves were used to determine the general shape of the two-photon signal for the given reference intensity and the effect of varying the sample's temperature. The position of the peak in two-photon photocurrent occured at the point where the reference intensity began to drop off, in the same manner as the experimental curves. Furthermore, the position of the peak was found to shift toward higher energies as the temperature was lowered, due to an increase in the energy gap.

Finally, Figure V.16 attempts to reproduce the experimental photocurrent with a sum of one and two-photon absorption signals at 88 K. To begin with, the one-photon signal was assumed to be directly proportional to the reference intensity. The two-photon signal was then arbitrarily multiplied by a constant. This factor was adjusted so that the maximum two-photon signal was equal to 50% of the maximum in the one-photon signal. The two contributions were then added to produce the curve shown in Figure V.16. The chosen ratio would correspond to a situation where the one-photon effect dominated, yet the two-photon contribution to the photocurrent was large enough to produce a significant change in the resulting curve.

The model reinforces the interpretation of the signal as being due to two-photon absorption in Cu_2O. The experimentally observed photocurrent can be reproduced by a weighted sum of the one and two-photon signals, with the relative contribution of the two-photon signal increasing as the bias voltage is increased. The two signals are added because the one-photon signal produced by the photoexcitation of holes from copper is of the same polarity as the two-photon signal produced by the Cu_2O conduction band electrons.

This brings the chapter to a close. The final chapter will briefly resume the work done and discuss future experiments.

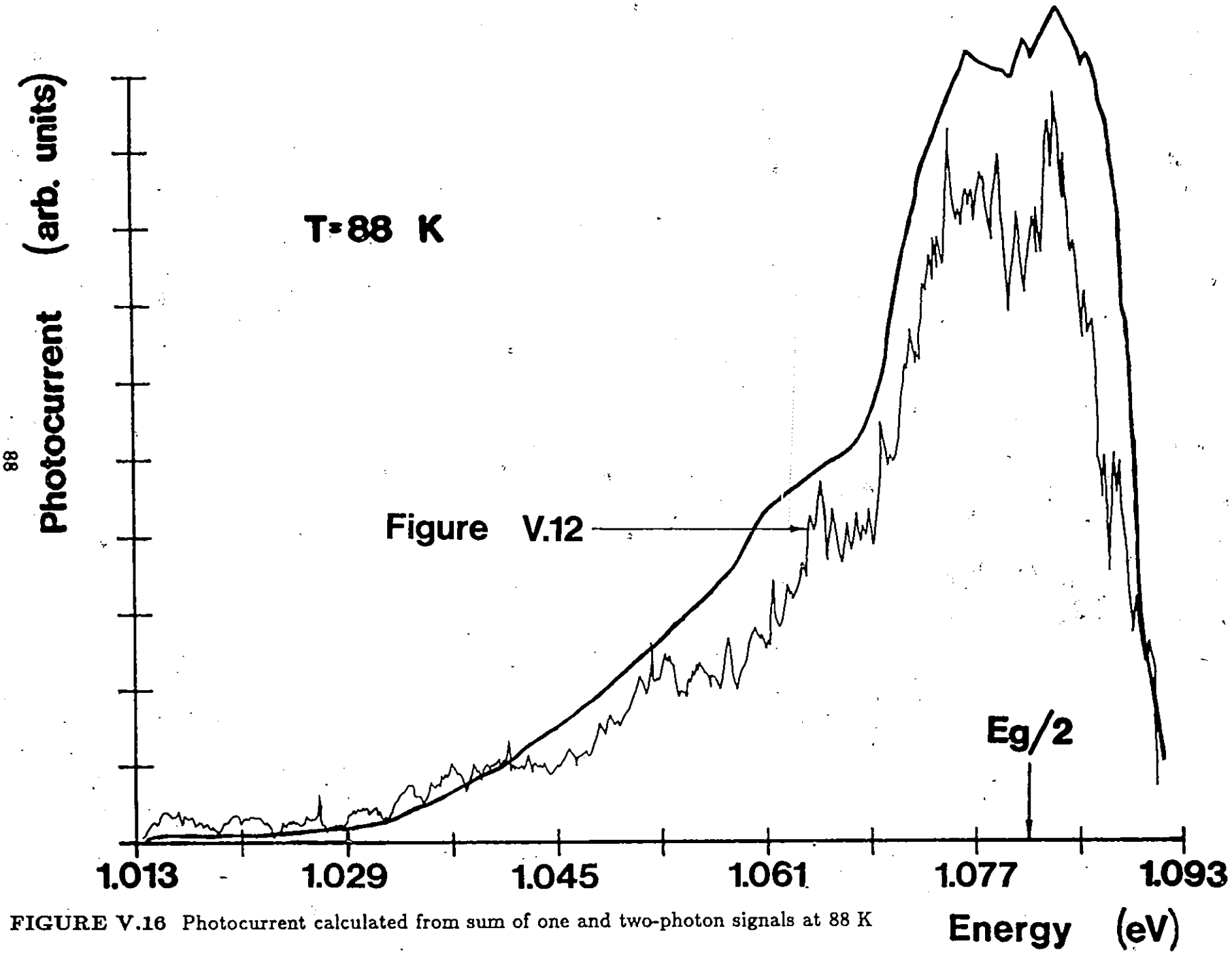

FIGURE V.16 Photocurrent calculated from sum of one and two-photon signals at 88 K

CHAPTER VI SUMMARY AND CONCLUSIONS

The aim of this work was the study of the exciton region of cuprous oxide using two-photon absorption. An optical parametric oscillator was recalibrated to narrow its linewidth when emitting at energies corresponding to those of the Cu_2O exciton region. The photovoltaic effect in Cu_2O/Cu Schottky barrier cells was used to detect the two-photon absorption. The photocurrent versus energy measurements performed at high intensity displayed structure that was attributed to two-photon absorption. Attempts to resolve individual exciton lines likely failed because of an insufficiently narrow infrared linewidth. A model of two-photon band-to-band absorption reproduced the observed structure.

Possible improvements to the existing setup would be the introduction of the etalon into the CMX/4 laser cavity which would decrease the resulting infrared linewidth by a factor of 4 with a minimal loss in output power. However, it is questionable whether or not the exciton lines could be resolved under the new conditions. A different source providing a greater peak intensity and narrower linewidth would probably produce better results. The problem consists in finding a tunable pulsed source that emits in the region of 1.15 μm. Dyes emitting in this region are available but are not easy to work with because they are highly toxic.

In my opinion, future attempts should be directed at measuring the two-photon transmission of single crystals of Cu_2O in the region of the n=1S exciton energy. Because it is located roughly 0.14 eV from the conduction band, the transmission characteristics of the sample should be flat in this area. It should then be readily obvious whether or not the

parametric oscillator can be used to resolve the n=1S exciton line as well as the rest of the series. The n=1S exciton's high binding energy would inhibit the use of the photovoltaic effect to determine this. Operating the parametric oscillator at a temperature slightly lower than 370°C would center the peak infrared intensity on the position of the n=1S line. This, and the use of a pyroelectric detector to measure the transmitted intensity are the only changes that would be required to the existing setup.

Despite not having been able to resolve the exciton lines, the photovoltaic effect is a viable technique by which to observe two-photon absorption in Cu_2O. Further development of the exciting source will be required so that transitions to the individual exciton levels can be observed.

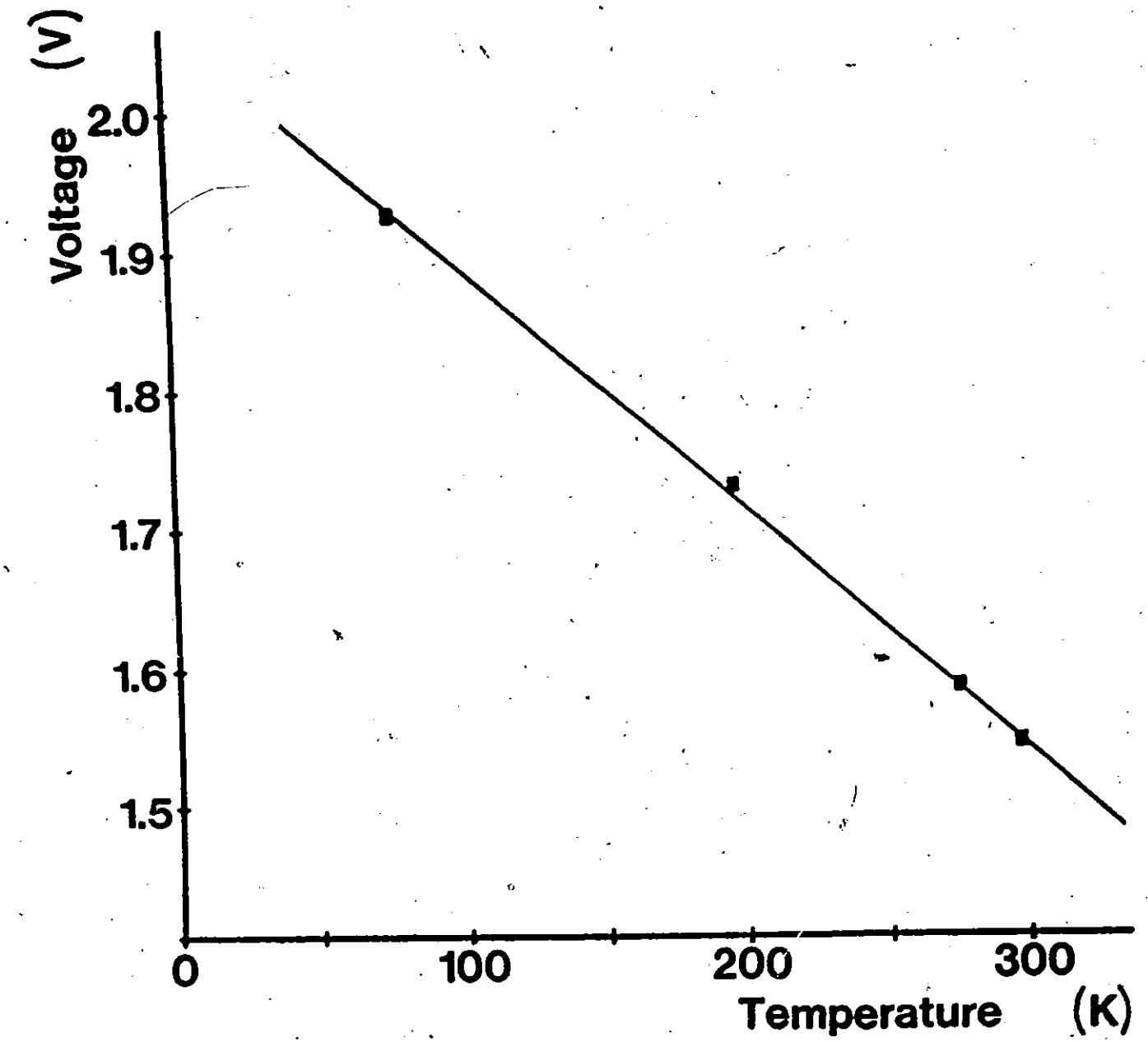

APPENDIX A Curve of forwafd bias voltage required to maintain a current of 1 mA through a Litton 209 diode

REFERENCES

1. M.F. Mott, Proc. R. Soc. London, **171**, 27 (1939)
2. L.C. Olsen, F.W. Addis and W. Miller, Solar Cells, **7**, 247 (1982-1983)
3. J. Frenkel, Phys. Rev., **37**, 17 (1931)
4. R. Peierls, Ann. Phys., **13**, 905 (1932)
5. V.T. Agekyan, B.S. Monozon and I.P. Shiryapov, phys. stat. sol. (b), **66**, 359 (1974)
6. R.J. Elliot, Phys. Rev., **108**, 1384 (1957)
7. S. Nikitine, Proc. Semiconductors, **6**, 233 (1962)
8. D. Fröhlich, R. Kenklies, Ch. Uihlein and C. Schwab, Phys. Rev. Lett., **43**,1260 (1979)
9. V.T. Agekyan, Phys. Stat. Sol. (a), **43**, 11 (1977)
10. R. Braunstein, Phys. Rev., **125**, 475 (1962)
11. D. Fröhlich and M. Sondergeld, J. Phys. E: Sci. Instr., **10**, 764 (1977)
12. Ch. Uihlein, D. Fröhlich and R. Kenklies, Phys. Rev. B, **23**, 2731 (1981)
13. V. Nathan, A.H. Guenther and S.S. Mitra, J. Opt. Soc. Am. B, **2**, 294 (1985)
14. K. C. Rustagi, F. Pradère and A. Mysyrowicz, Phys. Rev. B, **8**, 2721 (1973)
15. H.S. Brandi and Cid B. de Araùjo, J. Phys. C.: Solid State Phys., **16**, 5929 (1983)
16. H.D. Jones and H.R. Reiss, Phys. Rev. B, **16**, 2466 (1977)
17. P.L. Rochon, Ph.D. Thesis, U. of Ottawa, 1976
18. J. Robertson, Phys. Rev. B, **28**, 3378 (1983)
19. D.C. Reynolds and T.C. Collins, Excitons: Their Properties and Uses, p. 106 (Academic Press, New York, 1981)
20. J.P. Wolfe and A. Mysyrowicz, Sci. Am., **250**, 98 (1984)
21. J.C. Merle, S. Nikitine and H. Haken, Phys. Stat. Sol. (b), **61**, 229 (1974)
22. S. Nikitine, Optical Properties of Solids, Chapter 9, edited by S. Nudelman and S.S. Mitra, Plenum Press (1969)
23. E.F. Gross, Nuovo Cimento Suppl. **3**, 672 (1956)
24. J.A. Assimos and D. Trivich, J. Appl. Phys., **44**, 1687 (1973)
25. R.S. Knox, Theory of Excitons, Solid State Physics Supplement 5 (Academic Press, New York, 1963)
26. R.S. Zucker, J. Electrochem. Soc., **112**, 417 (1965)
27. R.S. Toth, R. Kilkson and D. Trivich, J. Appl. Phys., **31**, 1117 (1960)
28. Y. Ebisuzaki, J. Appl. Phys., **32**, 2027 (1961)
29. M. Grosmann, J. Chim. Phys., **62**, 1129 (1965)
30. D. Trivich and G.P. Pollack, J. Electrochem. Soc., **117**, 344 (1970)
31. A. Kinoshita and T. Nakano, Japan J. Appl. Phys.,**6**, 656 (1967)
32. J.H. Wernick and H.M. Davis, J. Appl. Phys., **27**, 149 (1956)
33. W.J. McG. Tegart, Electrolytic and Chemical Polishing of Metals (Pergamon Press, New York, 1956)
34. E. Fortin and W.M. Sears, Can. J. Phys., **60**, 901 (1982)
35. B.G. Cohen, W.B. Snow and A.R. Tretola, Rev. Sci. Instr., **34**, 1091 (1963)

36. R.L. Byer, Quantum Electronics, Chapter 9, edited by H. Rabin and C.L. Tang (Academic Press, New York, 1975)
37. CMX-4/IR Users' Guide
38. M.V. Hobden and J. Warner, Phys. Lett., **22**, 243 (1966)
39. F.L. Weichman and J.M. Reyes, Can. J. Phys., **58**, 325 (1980)
40. M. Tapiero, C. Noguet, J.P. Zielinger, C. Schwab and D. Pierrat, Rev. Phys. Appl., **14**, 231 (1979)
41. J. Seymour, Electronic Devices and Components, p. 77-79 (Pitman Publishing Ltd, London, 1981)
42. R.D. Schmidt-Whitley, M. Martinez-Clemente and A. Revcolevschi, J. Crystal Growth, **23**, 113 (1974)
43. Oxford Instruments CF204 Cryostat Operator's Manual
44. R.L. Powell, M.D. Bunch and R.J. Corruccini, Cryogenics (March 1961)